Columbia preprint CU–TP–756

The Time–Delay Signature of Quark–Gluon–Plasma Formation in Relativistic Nuclear Collisions †

Dirk H. Rischke and Miklos Gyulassy

Physics Department, Pupin Physics Laboratories, Columbia University
538 W 120th Street, New York, NY 10027, U.S.A.

June 1996

Abstract

The hydrodynamic expansion of quark–gluon plasmas with spherical and longitudinally boost-invariant geometries is studied as a function of the initial energy density. The sensitivity of the collective flow pattern to uncertainties in the nuclear matter equation of state is explored. We concentrate on the effect of a possible finite width, $\Delta T \sim 0.1\,T_c$, of the transition region between quark–gluon plasma and hadronic phase. Although slow deflagration solutions that act to stall the expansion do not exist for $\Delta T > 0.08\,T_c$, we find, nevertheless, that the equation of state remains sufficiently soft in the transition region to delay the propagation of ordinary rarefaction waves for a considerable time. We compute the dependence of the pion–interferometry correlation function on ΔT, since this is the most promising observable for time-delayed expansion. The signature of time delay, proposed by Pratt and Bertsch, is an enhancement of the ratio of the inverse width of the pion correlation function in out–direction to that in side–direction. One of our main results is that this generic signature of quark–gluon plasma formation is rather robust to the uncertainties in the width of the transition region. Furthermore, for longitudinal boost-invariant geometries, the signal is likely to be maximized around RHIC energies, $\sqrt{s} \sim 200$ AGeV.

† This work was supported by the Director, Office of Energy Research, Division of Nuclear Physics of the Office of High Energy and Nuclear Physics of the U.S. Department of Energy under Contract No. DE-FG-02-93ER-40764.

1 Introduction

Lattice calculations of the thermodynamical functions of quantum chromodynamics (QCD) indicate [1] that, (at zero net baryon density) in the vicinity of a critical temperature $T_c \sim$ 160 MeV, strongly interacting matter undergoes a rapid transition from a (chirally broken, confined) hadronic phase to a (chirally symmetric, deconfined) quark–gluon plasma (QGP). The width of that transition region is presently only known to be in the range $0 \leq \Delta T < 0.1\, T_c \sim 16$ MeV. Therefore, one cannot yet conclude whether the transition is a first order phase transition ($\Delta T = 0$), or merely a rapid increase of the entropy density associated with the change from d_H hadronic to d_Q quark and gluon degrees of freedom.

One of the primary goals of relativistic heavy-ion physics is the creation and experimental observation of the predicted QGP phase of matter. Many signatures have been proposed such as electromagnetic radiation of thermal dileptons and photons [2], J/Ψ–suppression [3], jet quenching [4], strangelet formation [5], or disordered chiral condensates (DCC's) [6]. These signatures, however, do not depend directly on the actual form of the nuclear matter equation of state. Thermal electromagnetic radiation is, for instance, generic to any hot system, independent from its degrees of freedom (as long as they have electromagnetic charge). For example, it was shown [7] that a hot hadron gas shines as brightly as a QGP. Similarly, jet quenching and J/Ψ–suppression[1] are generic consequences of final state interactions in any form of dense matter [9]. Finally, strangelet or DCC formation require very specific assumptions about the dynamical evolution of the system.

It is therefore of interest to study signals that are more directly related to the QCD equation of state. Signals of this type emerge from the influence of the equation of state on the *collective* dynamical evolution of the system. Such signals must be calculated within the framework of relativistic hydrodynamics [10], since that is the only dynamical model which provides a *direct* link between collective observables and the equation of state. Of course, the use of such an approach requires a strong dynamical assumption, namely that the equilibration rates are much larger than typical gradients of thermodynamic quantities in the system. It now appears that radiative gluon energy loss in a QGP may be sufficiently large [11] to support local equilibration on time scales less than 1 fm/c. In the following, we therefore neglect dissipative effects and assume the validity of ideal hydrodynamics to compute the collective evolution of the system.

It was shown in [12, 13, 14] that the transition to the QGP softens the equation of state in the transition region, and thus reduces the tendency of matter to expand on account of its internal pressure. This, in turn, delays the expansion and considerably prolongs the lifetime of the system. In [15, 16] it was moreover shown that this effect leads to a reduction of the transverse directed flow in semi-peripheral collisions that can be readily tested experimentally at fixed target energies [17].

In [14] the flow structure for the one–dimensional expansion of a slab of matter ("Landau expansion model" [18]) was studied as a function of its initial energy density ϵ_0 and of the width ΔT of the transition region in the equation of state. In particular, it was shown how,

[1] Renewed interest in that signature, has, however, emerged with the advent of recent results from the NA50 experiment at the CERN SPS, showing a rapid variation of J/Ψ–suppression as a function of transverse energy in Pb+Pb–collisions at 158 AGeV [8].

in addition to the softening of the equation of state, for $\Delta T < \Delta T^* \simeq 0.07676\, T_c$ the type of the hydrodynamical expansion solution changes qualitatively from a simple rarefaction wave to a rarefaction discontinuity. Such deflagration fronts [19] have small velocities, $v_{\rm d} \ll c$, and thus the conversion of QGP matter into hadronic matter is considerably delayed. In [14] we also showed that for larger transition widths ($\Delta T > \Delta T^*$) the lifetime of matter with temperature around T_c is considerably reduced but cooler regions with $T \sim 0.7\, T_c$ remain long-lived.

In the present work we extend the investigations of [14] to more realistic, 3–dimensional geometries. We consider systems with spherical symmetry ("fireball" geometry), and with transverse cylindrical symmetry and boost-invariant initial conditions in longitudinal direction ("Bjorken cylinder" geometry [20]). For these symmetric geometries it is possible to use a modified one–dimensional algorithm as e.g. presented in [13]. Note that in contrast to the simple one–dimensional Landau geometry, single inclusive particle spectra and also two–particle correlation functions can be calculated in a realistic way from the hydrodynamic solutions for the above geometries.

In this paper we show that the influence of the width ΔT of the transition on the dynamical evolution of the system in these 3–dimensional geometries is very similar to that found in [14] for purely one–dimensional expansion. In particular, the softening of the equation of state associated with a rapid cross-over region leads to a delay in the expansion and a prolonged lifetime of matter with temperature *below* T_c.

To explore observable consequences of the prolonged lifetime of the system, we then calculate the inverse width of the two–particle correlation functions in side– and out–direction, $R_{\rm side}$ and $R_{\rm out}$. We demonstrate that the initial energy density dependence of the system's lifetime is mapped closely by the excitation function of the ratio $R_{\rm out}/R_{\rm side}$. The phase transition leads to a time-delayed expansion that is reflected in an enhancement of the above ratio relative to its value obtained in the ideal gas case without a transition. This signature of the QGP transition was first proposed by Pratt [21] who performed similar calculations for the fireball geometry[2] and, independently, by Bertsch et al. [22] who employed a kinetic model for the hadronization in the Bjorken cylinder geometry. These previous investigations assumed the existence of a sharp first order transition, $\Delta T = 0$. We show here that this signature is a generic feature of a rapid cross-over transition and holds for $\Delta T = 0.1\, T_c$ as well.

The importance of the time delay as a signature of QGP formation is that it is among the few signatures that probe directly the equation of state of strongly interacting matter. It tests whether there exists a "soft region" in the equation of state of ultra-dense matter [12] which is most naturally characterized [14] by a reduction of the local velocity of sound c_S as a function of the local energy density. As discussed in detail in the next section, a very general feature of a transition (that happens within a sufficiently narrow temperature interval ΔT) is the existence of such a region. For matter passing through that region of energy densities during the expansion phase, the flow will temporarily slow down or even possibly stall under suitable conditions. The main result of the present work is to identify initial conditions where

[2]Pratt's method to solve the hydrodynamical equations and to calculate the correlation functions differ in important aspects from our approach, but our final results for the correlation functions turn out to be rather similar to his.

the resulting stall is sufficiently long to be observable via pion interferometry [21, 22]. As we show, the maximum time delay may occur at AGS as well as at RHIC energies, depending on whether matter is initially stopped in a fireball or expands as in Bjorken's longitudinally boost-invariant scenario.

The remainder of this paper is organized as follows. In Section 2 we present the equation of state used in our investigations and explain our method to solve the hydrodynamical equations numerically for the above mentioned geometries. In Section 3 we compare the hydrodynamical expansion solutions for different initial energy densities, for different values of ΔT, and for different values of degrees of freedom in the QGP and hadronic phase. Section 4 is devoted to the discussion of the lifetime of the system and how it can be measured via the widths of the side– and out–correlation function. Section 5 concludes with a summary and discussion of our results. Two Appendices contain the derivation of the formulae employed to calculate the two–particle correlation functions in the hydrodynamical framework. Natural units $\hbar = c = k_B = 1$ are used throughout this paper.

2 Equation of State and Hydrodynamics

Available lattice data for the entropy density in full QCD can be approximated by the simple parametrization [14, 23]

$$\frac{s}{s_c}(T) = \left[\frac{T}{T_c}\right]^3 \left(1 + \frac{d_Q - d_H}{d_Q + d_H} \tanh\left[\frac{T - T_c}{\Delta T}\right]\right) , \tag{1}$$

where $s_c = const. \times \frac{1}{2}(d_Q + d_H)\, T_c^3$ is the entropy density at T_c. Pressure p and energy density ϵ follow then from thermodynamical relationships. For $\Delta T = 0$, the equation of state (1) reduces to the MIT bag equation of state [24] with bag constant $B = \frac{1}{2}(d_Q/d_H - 1)\, T_c\, s_c/\,(d_Q/d_H + 1)$. If one measures energies in units of T_c and energy densities in units of the enthalpy density $\epsilon_c + p_c = T_c\, s_c$, the equation of state (1) depends only on the ratio d_Q/d_H, and not on d_Q and d_H separately. For $\Delta T = 0$, this ratio determines the latent heat (density) $\epsilon_Q - \epsilon_H \equiv 4B$. (Here, $\epsilon_Q = \frac{1}{2}(4\, d_Q/d_H - 1)\, T_c\, s_c\,/\,(d_Q/d_H + 1)$ is the energy density at the phase boundary between mixed phase and QGP, $\epsilon_H = \frac{3}{2}\, T_c\, s_c\,/\,(d_Q/d_H + 1)$ is that at the boundary between mixed and hadronic phase.)

For the case $d_H = 3$ (corresponding to an ultrarelativistic gas of pions) and $d_Q = 37$ (corresponding to two massless flavours of quarks and antiquarks, and eight massless gluons), the latent heat, $4B = 1.7\, T_c\, s_c \simeq 1.272$ GeV fm^{-3}, is large. On the other hand, including a resonance gas in the hadronic phase and/or reducing the effective number of degrees of freedom on the QGP side [25], $d_Q/d_H = 3$ may be taken as a (perhaps more realistic) lower limit, with a smaller latent heat $\epsilon_Q - \epsilon_H = T_c\, s_c$. Assuming that the high-temperature phase consists of gluons only (such as expected for the "hot-glue scenario" [26]) this would then correspond to about 400 MeV fm^{-3} in physical units. To cover the range of uncertainty in the QCD equation of state we consider $d_Q/d_H = 37/3$ and $d_Q/d_H = 3$, and $\Delta T = 0$ and $0.1\, T_c$ in our investigation of hydrodynamical expansion solutions.

In Fig. 1 we show (a) the entropy density and (b) the energy density as functions of temperature, and (c) the pressure and (d) the velocity of sound squared $c_S^2 \equiv \mathrm{d}p/\mathrm{d}\epsilon$ as

functions of energy density for $\Delta T = 0,\, 0.1\, T_c$, and an ideal gas with d_H degrees of freedom for $d_Q/d_H = 37/3$. The corresponding plot for $d_Q/d_H = 3$ looks rather similar qualitatively and is not shown. Quantitative differences are: (i) the phase boundaries are different, ϵ_Q shifts from $1.8125\, T_c\, s_c$ to $1.375\, T_c\, s_c$, ϵ_H from $0.1125\, T_c\, s_c$ to $0.375\, T_c\, s_c$, and p_c from $0.0375\, T_c\, s_c$ to $0.125\, T_c\, s_c$. Also, as mentioned above, (ii) the latent heat $\epsilon_Q - \epsilon_H$ is reduced.

Figs. 1 (a,b) present the thermodynamic functions in a form to facilitate comparison with lattice data. Present lattice data for full QCD can be approximated with a choice of ΔT in the range $0 \leq \Delta T < 0.1\, T_c$. In the hydrodynamical context, however, Figs. 1 (c,d) are more relevant. As can be seen in (c), for $\Delta T = 0$ the pressure stays constant, $p_c = \frac{1}{2}\, T_c\, s_c \,/\, (d_Q/d_H + 1)$, in the mixed phase $\epsilon_H \leq \epsilon \leq \epsilon_Q$. Hydrodynamical expansion is, however, driven by pressure *gradients*. It is therefore the velocity of sound, Fig. 1 (d), that is the most relevant measure of the system's tendency to expand. It represents the capability to perform mechanical work (which is proportional to pressure gradients dp) for a given gradient in energy density dϵ. For $\Delta T = 0$, the velocity of sound vanishes in the mixed phase, i.e., mixed phase matter does not expand at all on its own account, even if there are strong gradients in the energy density. This has the consequence that it does not perform mechanical work and therefore cools less rapidly. For finite ΔT, pressure gradients are finite, but still smaller than for an ideal gas equation of state, and therefore the system's tendency to expand is also reduced, cf. Fig. 1 (d).

Hydrodynamics is defined by local energy–momentum conservation,

$$\partial_\mu T^{\mu\nu} = 0 \ . \tag{2}$$

Under the assumption of local thermodynamical equilibrium (the so-called "ideal fluid" approximation) the energy–momentum tensor $T^{\mu\nu}$ assumes the particularly simple form [27]

$$T^{\mu\nu} = (\epsilon + p)\, u^\mu u^\nu - p\, g^{\mu\nu} \ , \tag{3}$$

where $u^\mu = \gamma\,(1, \mathbf{v})$ is the 4–velocity of the fluid ($\mathbf{v}$ is the 3–velocity, $\gamma \equiv (1 - \mathbf{v}^2)^{-1/2}$, $u_\mu u^\mu = 1$), and $g^{\mu\nu} = \mathrm{diag}(+,-,-,-)$ is the metric tensor. The system of equations (2) is closed by choosing an equation of state in the form $p = p(\epsilon)$, i.e., as depicted in Fig. 1 (c). In the ideal fluid approximation, the (equilibrium) equation of state is the *only* input to the hydrodynamical equations of motion (2) that relates to properties of the matter under consideration and is thus able to influence the dynamical evolution of the system. The final results are uniquely determined once a particular initial condition and a decoupling ("freeze-out") hypersurface are specified.

The symmetry of the fireball and Bjorken cylinder geometry affects that the system of four equations (2) reduces to two independent equations. With the definition $E \equiv T^{00}$, $M \equiv T^{0r}$, where the index r indicates the radial component of the energy–momentum tensor, the respective equations read

$$\partial_t\, E + \partial_r\, [(E + p)v] \ = \ -\, F(E, p, v, r, t) \ , \tag{4}$$

$$\partial_t\, M + \partial_r\, (Mv + p) \ = \ -\, G(M, v, r, t) \ . \tag{5}$$

Here, v is the radial component of the velocity. For the fireball geometry, F and G do not

depend on the time t explicitly,

$$F_{\rm fb}(E,p,v,r) = \frac{2\,v}{r}\,(E+p)\ , \quad G_{\rm fb}(M,v,r) = \frac{2\,v}{r}\,M\ . \tag{6}$$

For the Bjorken cylinder geometry, the above equations describe the system's transverse evolution at $z = 0$ (cf. [28]), and due to the assumption of longitudinal boost invariance [20], the hydrodynamical solution for arbitrary z can be easily obtained by a Lorentz boost with (space–time) rapidity $\eta = \mathrm{Artanh}\,[z/t]$. The functions F and G read in this case

$$F_{\rm Bj}(E,p,v,r,t) = \left(\frac{v}{r}+\frac{1}{t}\right)(E+p)\ , \quad G_{\rm Bj}(M,v,r,t) = \left(\frac{v}{r}+\frac{1}{t}\right)M\ . \tag{7}$$

In order to solve (4,5), we employ Sod's operator splitting method [29], i.e., for each time step we first generate solutions of the hydrodynamical equations for $F = G = 0$. In this form, the equations are purely one–dimensional and can therefore be solved with e.g. the relativistic HLLE scheme presented in [13, 30]. The performance of this algorithm for solving one–dimensional hydrodynamical problems and with equations of state featuring phase transitions was shown to be excellent [13, 31]. It has also been employed in [14] to solve the Landau expansion problem.

In a second step, Sod's method prescribes to correct E and M for the respective geometry by solving the ordinary differential equations

$$\frac{{\rm d}E}{{\rm d}t} = -F(E,p,v,r,t)\ , \quad \frac{{\rm d}M}{{\rm d}t} = -G(M,v,r,t)\ . \tag{8}$$

More specifically, in a slight variation of Sod's method we solve the finite difference equations

$$E = \tilde{E} - F(\tilde{E},\tilde{p},\tilde{v},r,t)\,{\rm d}t\ , \quad M = \tilde{M} - G(\tilde{M},\tilde{v},r,t)\,{\rm d}t\ , \tag{9}$$

where quantities with a tilde are the solutions of the hydrodynamical equations with $F = G = 0$ generated previously with the relativistic HLLE scheme. This two–step predictor–corrector scheme is repeated for each time step to obtain the complete time evolution of the system.

Fig. 2 shows temperature and laboratory energy density profiles calculated with Sod's method for the expansion of (a,b) a sphere and (c,d) a Bjorken cylinder (for initial time $t_0 \equiv \tau_0 = 0.1\,R$) with an ideal gas equation of state $p = \epsilon/3$ in comparison to profiles generated with the semi-analytic method of characteristics [28]. That method is a benchmark test for numerical algorithms as long as the hydrodynamical solution is continuous [13]. The grid spacing for the HLLE scheme is taken as $\Delta x = 0.01\,R$, the time step width for the HLLE scheme and the corrector step (9) is $\Delta t = 0.99\,\Delta x$. As one observes, agreement is excellent (even on a logarithmic scale) which gives confidence that Sod's method as described above works for the more complicated equation of state (1) as well (which leads to discontinuous hydrodynamical expansion solutions for $\Delta T < \Delta T^* \simeq 0.07676\,T_c$ [13]).

3 Expansion solutions

In this section we present the hydrodynamical expansion solutions for the fireball and Bjorken cylinder geometry for different initial energy densities ϵ_0. We assume ϵ_0 to be homogeneous throughout the system. We compare solutions for the equation of state (1) with $\Delta T = 0$ and $0.1\,T_c$ with solutions for an ideal gas of equation of state with d_H degrees of freedom. We explicitly show results for $d_Q/d_H = 37/3$ and, where necessary, comment on the difference to the case $d_Q/d_H = 3$. As in [14] we will use the notion "lifetime" for the intercept of a particular isotherm with the t–axis.

Note that in our comparison we fix the initial *energy density* rather than the initial temperature or entropy density, as sometimes assumed [32], because the latter are derived thermodynamic quantities while the former is determined by non-equilibrium energy loss mechanisms. For instance, at RHIC energies it is expected [26] that semi-hard perturbative QCD processes determine the initial energy density in the range $\epsilon_0 \sim 10 - 20$ GeV/fm^3.

3.1 Fireball geometry

This case is rather similar to the one–dimensional Landau expansion studied in [14]. Differences are solely due to the spherical geometry (i.e., due to the extra terms (6) in the equations of motion).

In Fig. 3 we show temperature profiles and isotherms in the $t - r$ plane for $\epsilon_0 = \epsilon_H = 0.1125\,T_c\,s_c$. Of course, for this initial energy density, the case $\Delta T = 0$ (a,b) is identical to the ideal gas case (e,f). Note the delayed expansion in the case $\Delta T = 0.1\,T_c$, Figs. 3 (c,d), due to the reduction in the velocity of sound, cf. Fig. 1 (d). This is quite similar to the one–dimensional expansion (cf. Figs. 3 (c,i) of Ref. [14]), although the overall scale of the lifetimes is now considerably reduced since the system has two more spatial dimensions into which it can expand.

Fig. 4 shows the situation for an initial energy density $\epsilon_0 = 1.875\,T_c\,s_c$ which is close to $\epsilon_Q = 1.8125\,T_c\,s_c$. As in the one–dimensional expansion (cf. Fig. 5 of [14]), the lifetime of the system is very long in the case $\Delta T = 0$, due to the small velocity of the deflagration front converting mixed phase matter into hadrons. As compared to the lifetime of the mixed phase in the one–dimensional expansion, $t_{\rm life} \sim 40\,R$ (cf. Fig. 5 (g) of [14]), that lifetime is now, however, only about $18\,R$, due to the more rapid expansion in three spatial dimensions. As in the one–dimensional case, cooling is faster for $\Delta T = 0.1\,T_c$ (cf. Fig. 5 (i) of [14]). While in that case, however, the lifetimes were only slightly shorter than for $\Delta T = 0$, now they are reduced by about a factor of 3. The fastest expansion is that for the ideal gas, in accord with the discussion of Fig. 1 (d).

In Fig. 5 the initial energy density is well above the mixed phase region, $\epsilon_0 = 18.75\,T_c\,s_c \sim 10\,\epsilon_Q$. As for the analogous one–dimensional expansion solution (Fig. 7 of [14]) the internal energy density and pressure are so large that, in the case of a transition to the QGP, Figs. 5 (a–d), the system explodes rather than burns slowly as in the preceding case, Fig. 4. Nevertheless, the expansion is still somewhat delayed as compared to the expansion of an ideal gas, Figs. 5 (e,f).

3.2 Bjorken cylinder geometry

For the discussion of the expansion in the Bjorken cylinder geometry it is instructive to first focus on purely longitudinal expansion. Longitudinal boost invariance with regard to boosts with $\eta = \mathrm{Artanh}\,[z/t]$ [20] implies that the longitudinal velocity is given by $v^z = z/t$. In turn, the longitudinal fluid rapidity is identical with the boost rapidity η. It is easy to show that in this case the hydrodynamical equations (2) reduce to

$$\partial_\tau \, \epsilon \,|_\eta = -\frac{\epsilon + p}{\tau} \ , \quad \partial_\eta \, p \,|_\tau = 0 \ , \tag{10}$$

where $\tau \equiv \sqrt{t^2 - z^2}$ is the proper time associated with fluid elements moving with $v^z = z/t$. The second equation implies that pressure gradients vanish along space–time hyperbolas $\tau = const.$ and, for baryon-free matter, that the temperature is constant on these hyperbolas. The first equation is an ordinary differential equation on the space–time hyperbolas and describes the cooling of the system on account of the longitudinal motion. For baryon-free matter, the thermodynamical identities $\mathrm{d}\epsilon = T\,\mathrm{d}s$ and $\epsilon + p = Ts$ imply the very simple cooling law

$$\partial_\tau \, s \,|_\eta = -\frac{s}{\tau} \ , \tag{11}$$

which has the solution $s(\tau) = s_0 \, [\tau/\tau_0]^{-1}$, *independent* from the underlying equation of state.

For an ultrarelativistic ideal gas equation of state $p = \epsilon/3$, $\epsilon = const. \times T^4$, the solution of the longitudinal boost-invariant expansion problem is

$$\epsilon(\tau) = \epsilon_0 \, [\tau/\tau_0]^{-4/3} \ , \quad T(\tau) = T_0 \, [\tau/\tau_0]^{-1/3} \ . \tag{12}$$

For the equation of state (1) with $\Delta T = 0$, one can easily solve (10) analytically. If $\epsilon_0 > \epsilon_Q$ we have

$$\epsilon(\tau) \ = \ \begin{cases} (\epsilon_0 - B) \, [\tau/\tau_0]^{-4/3} + B \ , & \tau_0 \le \tau \le \tau_Q \ , \\ (\epsilon_Q + p_c) \, [\tau/\tau_Q]^{-1} - p_c \ , & \tau_Q < \tau \le \tau_H \ , \\ \epsilon_H \, [\tau/\tau_H]^{-4/3} \ , & \tau > \tau_H \ , \end{cases} \tag{13}$$

$$T(\tau) \ = \ \begin{cases} T_0 \, [\tau/\tau_0]^{-1/3} \ , & \tau_0 \le \tau \le \tau_Q \ , \\ T_c \ , & \tau_Q < \tau \le \tau_H \ , \\ T_c \, [\tau/\tau_H]^{-1/3} \ , & \tau > \tau_H \ . \end{cases} \tag{14}$$

Here, $\tau_Q = \tau_0 \, [(\epsilon_Q - B)/(\epsilon_0 - B)]^{-3/4}$ is the (proper) time the system enters the mixed phase, and $\tau_H = \tau_Q \, d_Q/d_H$ the time corresponding to entry of the hadronic phase. Note that the time spent in the mixed phase is linear proportional to the ratio d_Q/d_H. Also, the system does not cool at all in this phase, $T = T_c = const.$, due to the fact that no mechanical work is performed (cf. the above discussion of Fig. 1 (d)). As another consequence, the energy density does not decrease with $\tau^{-4/3}$ as in the QGP and hadronic phase, but only proportional to τ^{-1}, precisely as in a (one–dimensional) free-streaming expansion (where no mechanical work is performed as well).

For $\epsilon_Q \geq \epsilon_0 > \epsilon_H$, the solution reads

$$\epsilon(\tau) = \begin{cases} (\epsilon_0 + p_c)\,[\tau/\tau_0]^{-1} - p_c\ , & \tau_0 \leq \tau \leq \tau_H\ , \\ \epsilon_H\,[\tau/\tau_H]^{-4/3}\ , & \tau > \tau_H\ , \end{cases} \tag{15}$$

$$T(\tau) = \begin{cases} T_c\ , & \tau_0 \leq \tau \leq \tau_H\ , \\ T_c\,[\tau/\tau_H]^{-1/3}\ , & \tau > \tau_H\ . \end{cases} \tag{16}$$

Here, $\tau_H = \tau_0\,(\epsilon_0 + p_c)/(\epsilon_H + p_c)$. For $\epsilon_0 \leq \epsilon_H$, the solution is identical to (12).

For finite ΔT there is, contrary to expectation, also a simple, semi-analytic solution which does *not* require to solve the equations of motion (10) explicitly. Due to the fact that the entropy density behaves as $s(\tau) = s_0\,[\tau/\tau_0]^{-1}$ irrespective of the equation of state, and since the equation of state (1) establishes (for finite ΔT) a one-to-one correspondence between temperature and entropy density, there is also a one-to-one correspondence between temperature and τ. Once $s(\tau)$ and $T(\tau)$ are known, one can easily calculate $\epsilon(\tau)$ and $p(\tau)$ from fundamental thermodynamical relationships.

For illustrative purposes, we show in Fig. 6 the time evolution of (a) energy density, (b) entropy density, (c) pressure, and (d) temperature assuming an initial energy density $\epsilon_0 = 10\,T_c\,s_c$ and $d_Q/d_H = 37/3$. Solid lines are for $\Delta T = 0$, dotted lines for $\Delta T = 0.1\,T_c$, and dashed lines for an ideal gas with d_H degrees of freedom. The change in the cooling law for the energy density when entering the mixed phase is clearly visible in Fig. 6 (a). Also, Fig. 6 (b) illustrates that the cooling law for the entropy density is independent from the equation of state, although the magnitude of the entropy density differs for the different equations of state because of our assumption of fixed initial energy density.

We mention that for $\Delta T = 0.1\,T_c$, the parts of the system with temperature $T > 0.8\,T_c$ cool *faster* than for the ideal gas, cf. Fig. 6 (d). Only parts cooler than $\sim 0.7\,T_c$ survive longer than in the ideal gas case. This is in agreement with the results of [14] for the Landau expansion model, where it was concluded that it is therefore less likely that electromagnetic radiation is a viable signature for the transition, in contrast to the conclusions of [12]. On the other hand, it was speculated in [14] (referring to the conclusions of [21, 22]) that, if the system freezes out at temperatures $\leq 0.7\,T_c$, the delayed expansion might be observable in side– and outwards radii of two–particle correlation functions. This indeed happens to be the case, as will be shown in the next section.

For given initial energy density ϵ_0 and proper time τ_0, one can ask the question, how much longer it takes a system described by the equation of state (1) to reach a certain freeze-out temperature $T_f \leq T_c$ in comparison to the expansion of an ideal gas (12). Since the ideal gas is supposed to freeze out at the same temperature T_f and to have d_H massless degrees of freedom, particle and entropy density at freeze-out are the same in both cases. For $\Delta T = 0$ one can easily answer this question analytically: for $\epsilon_0 \gg B$, the freeze-out time $\tau_f \equiv \tau(T_f)$ is prolonged by a factor $[d_Q/d_H]^{1/4}$. For $d_Q/d_H = 37/3$, the delay in cooling is about 87% (as one can also see in Fig. 6 (d)), for $d_Q/d_H = 3$ it is only about 32%. Note that this prolongation of the lifetime of the system is in agreement with the one for the Landau expansion model at very high initial energy densities (cf. [14] and Fig. 10 below). Only for initial energy densities around ϵ_Q is the prolongation of the lifetime larger in the Landau expansion (see Fig. 10) due to the fact that there exists a slow deflagration solution which

delays the expansion even further. Such a solution does not occur in the purely longitudinal Bjorken expansion.

This changes when we consider transverse motion as well. In the following we fix $\tau_0 = 0.1\,R$. This choice is motivated by the fact that for Au+Au collisions at RHIC, the transverse radius of the hot zone is of the order 5 fm, while the time scale of local equilibration is roughly given by the energy loss of a parton in strongly interacting matter, $\tau_{dE/dx} \sim 0.5$ fm [11]. We have, however, also considered the case $\tau_0 = 0.5\,R$ and $\tau_0 = 1/3\,T_0$ (which is motivated by an uncertainty principle argument) and will comment on differences to the choice $\tau_0 = 0.1\,R$ where necessary.

Let us first consider the case $\epsilon_0 = \epsilon_H = 0.1125\,T_c\,s_c$, cf. Fig. 7. Due to the strong initial longitudinal motion, the system cools rather quickly below temperatures of $0.5\,T_c$, even before the transverse rarefaction wave reaches the center of the cylinder. The lifetimes are therefore solely determined by the longitudinal scaling expansion. This causes the horizontal parts of the isotherms. For the $T = 0.5\,T_c$ isotherm and $\Delta T = 0$ one expects from eq. (16) the lifetime $t_{\,\mathrm{life}} = 0.5^{-3} \times\ 0.1R = 0.8\,R$, in good agreement with Figs. 7 (a,b,e,f). (Due to the numerical dissipation adherent to any finite difference scheme that solves the hydrodynamical equations, the system cools slightly faster in the numerical calculation, cf. Figs. 7 (b,f).) The effect of longitudinal cooling is reduced for larger values of τ_0, cf. (12). For instance, in the case $\tau_0 = 0.5\,R$ the center still has $T \simeq 0.6\,T_c$ when the transverse wave reaches it. The lifetimes for $T > 0.6\,T_c$ are therefore (as expected) a factor of 5 longer.

In Fig. 8 we show the situation for $\epsilon_0 = 1.875\,T_c\,s_c \sim \epsilon_Q$. As in the preceding case, it takes some time before the transverse expansion wave reaches the center. Thus, the lifetimes of the highest temperatures in the system are solely determined by the longitudinal scaling solution presented above (horizontal parts of the respective isotherms).

It is interesting to note that the lifetimes for $\Delta T = 0$ and this particular ϵ_0 are not that exceedingly long as they were in the case of one–dimensional and spherical expansion. These long lifetimes were due to the slow velocity of the deflagration front. A deflagration solution, however, exists only for energy densities in the mixed phase, where matter is thermodynamically anomalous [14]. Here, the strong longitudinal motion cools the system quickly below the respective energy densities, such that the transverse expansion proceeds as a (comparatively fast) simple rarefaction wave instead of the deflagration. Thus, the system cools even more quickly and the lifetimes are considerably reduced.

This effect is, however, compensated when higher initial energy densities are considered. In Fig. 9 we show the solutions for $\epsilon_0 = 18.75\,T_c\,s_c \sim 10\,\epsilon_Q$. This case is close to the initial conditions expected from mini-jet production at RHIC energies. Now the initial energy density is sufficiently high that for $\Delta T = 0$ the plasma enters the mixed phase at relatively late time ($\tau_Q \sim 3$ fm for $\tau_0 = 0.5$ fm, see also Fig. 6 (d)). Therefore, the time spent in the mixed phase is long enough in this case to allow a transverse deflagration front to form, cf. Figs. 9 (a,b). In comparison to the ideal gas case (e,f), where no such solution exists, the expansion is therefore considerably prolonged. Such a time delay is observed also for $\Delta T = 0.1\,T_c$, Figs. 9 (c,d), and is here due to the reduction of the velocity of sound in the transition region.

We note that for $\tau_0 = 0.5\,R$, the initial energy density where one observes this effect is smaller, $\epsilon_0 \sim 2 - 3\,\epsilon_Q$. On the other hand, for $\tau_0 = 1/3\,T_0$ the initial time decreases with

increasing initial energy density, enhancing the effect of longitudinal cooling, such that ϵ_0 has to be very high ($> 40\,\epsilon_Q$) for the onset of this effect. Then, however, a steady increase of the initial energy density affects a steady decrease of τ_0 such that one observes a prolongation of the lifetimes over a wider range of energy densities (see also Fig. 13 below). It is furthermore interesting to note that this phenomenon occurs at about the same initial energy densities (in units of $T_c\,s_c$) in the case $d_Q/d_H = 3$ (cf. Fig. 12).

Finally, for very high energy densities, one recovers the case of the violent explosion, and the lifetimes are again reduced. This happens at lower initial energy densities for the case $\tau_0 = 0.5\,R$, since the longitudinal motion is less effective in cooling the system. For $\tau_0 = 1/3\,T_0$ we have not found a decrease in the lifetime up to the highest initial energy density studied by us, $\epsilon_0 = 300\,T_c\,s_c$. The reason is, as mentioned above, that the increasingly more efficient cooling due to longitudinal motion compensates the increasing tendency of the system to explode transversally.

4 Lifetimes and two–particle correlations

In this section we first discuss the lifetimes of differently hot parts of the system (defined as the intercept of a particular isotherm with the t–axis) as a function of the initial energy density. Assuming that the system freezes out at these temperatures, we then show how the lifetimes can be inferred from two–particle correlation functions.

4.1 Lifetimes

For convenience, we first show in Fig. 10 the lifetimes as a function of ϵ_0 for the one–dimensional (Landau) expansion studied in [14]. Figs. 10 (a) and (b) are for the case $d_Q/d_H = 37/3$, (c) and (d) are for $d_Q/d_H = 3$. The thick lines in (a,c) show the lifetimes of matter with $T = 0.7\,T_c$ (solid line), $T = 0.9\,T_c$ (dotted), and $T = T_c$ (dashed) for $\Delta T = 0$, the corresponding lines in (b,d) are for finite $\Delta T = 0.1\,T_c$. For comparison, the thin lines are the corresponding lifetimes for the expansion of an ideal gas with d_H degrees of freedom (they are identical in (a) and (b) as well as in (c) and (d)).

One clearly observes the maximum in the lifetime of mixed phase matter ($T = T_c$) at $\epsilon_0 = \epsilon_Q$ in Figs. 10 (a,c). As discussed in [14], this maximum vanishes for finite ΔT, Figs. 10 (b,d). Moreover, such hot matter does not survive as long as in the ideal gas case. The lifetime of cooler matter with $T = 0.7\,T_c$, however, stays longer than in the expansion of an ideal gas, independent of the value of ΔT. Note the change in the scale of $t_{\,\mathrm{life}}$ by a factor of 3 between (a,b) and (c,d). This is due to the reduction of the latent heat for a smaller ratio d_Q/d_H, which in turn accelerates the expansion.

Fig. 11 shows the corresponding diagram for the spherical expansion. First of all, one notices that, at high ϵ_0, there is almost no difference between the lifetime of a system with a transition to the QGP and an ideal gas. Inspecting Fig. 5, one observes, however, that the bulk of matter at finite r does indeed live longer in the first case. Thus, for the spherical expansion, our definition of 'lifetime' should rather be replaced by an average over the particular isotherm. It is, however, not necessary to do so at this point, since the correlation

functions considered subsequently will take this into account in a natural way.

Second, one observes that the lifetimes do not grow as strongly for high ϵ_0 as in the one–dimensional expansion. This is due to the fact that the system disperses its initial internal energy much more efficiently into kinetic energy in three dimensions than it does in one dimension. This also leads to the reduction of the overall scale in the lifetimes as compared to Fig. 10.

Third, it is noticeable that the *increase* of the lifetime for $\Delta T = 0$ at $\epsilon_0 = \epsilon_Q$ (where the lifetime is maximum) as compared to the ideal gas case is about a factor of 2 bigger than in the one–dimensional expansion. The prolongation of the lifetime is thus most pronounced in spherical geometry. Unfortunately, the reduction of the lifetime in the case of a smooth transition is also rather strong, cf. Figs. 11 (b,d). Nevertheless, for freeze-out at $T = 0.7\,T_c$ the lifetime can still be longer by a factor of 2 in the case of a transition than in the expansion of an ideal gas. Moreover, in contrast to the one–dimensional case, the spherical geometry leads to a (broad) maximum in the lifetime around ϵ_Q.

In Fig. 12 we present the lifetimes for the expansion of a Bjorken cylinder with initial time $\tau_0 = 0.1\,R$. One still observes the distinguished maximum in the lifetime associated with the transition to the QGP as seen in the preceding Fig. 11. In this case, however, the overall scale is even smaller (due to the fact that the system is from the very beginning quite effectively diluted by the longitudinal velocity field).

Moreover, one observes a shift in the maximum of the lifetime. This was discussed in the preceding section and is due to the fact that the longitudinal motion compensates the tendency to explode transversally (on account of a high initial energy density). For $\Delta T = 0$ the maximum is now around $\epsilon_0 \sim 20 - 50\,T_c\,s_c$ for *both* values of d_Q/d_H. For $\Delta T = 0.1\,T_c$, one still observes a maximum in the lifetimes, but as in Fig. 11 it is also broader and less pronounced.

The corresponding plot for $\tau_0 = 0.5\,R$ looks rather similar, and will therefore not be shown here. The position of the maximum is, however, shifted to smaller $\epsilon_0 \sim 3 - 7\,T_c\,s_c$, for reasons discussed above. The situation for a dynamical $\tau_0 = 1/3\,T_0$ is shown in Fig. 13. As one expects from the above discussion, there is a steady increase of the lifetime up to the highest considered ϵ_0.

4.2 Two–particle correlation functions

To calculate two–particle correlation functions we use the method developped by Pratt [21], Sinyukov [33] and others, and applied to hydrodynamics by the Marburg group [34]. This method is essentially a straightforward generalization of the Cooper–Frye formula [35] for single inclusive particle spectra to the case of correlation functions.

To calculate single inclusive particle spectra or two–particle correlation functions in the hydrodynamical framework, one assumes that a fluid element decouples from the fluid evolution ("freezes out") as soon as the particle density drops below a certain critical value where the collision rate becomes too small to maintain (local) thermodynamical equilibrium. In our case, the particle density depends on the temperature T only. Therefore, freeze-out happens across isotherms in the space–time diagram. To incorporate the freeze-out consistently into the solution of the hydrodynamical equations is a non-trivial problem. Hydrodynamics is

obviously not applicable to determine the motion of particles that are already frozen out. Therefore, the hydrodynamical solution has to be restricted to a limited region of space–time. The main difficulty is that its boundary, i.e., the freeze-out hypersurface, has to be determined *dynamically*, i.e., simultaneously with the solution of the hydrodynamical equations. A possible treatment of this problem was recently proposed by Bugaev [36], but has so far not been applied in practical calculations.

Commonly one circumvents this problem assuming the validity of the hydrodynamical description in the *whole* forward light cone, then solves the hydrodynamical equations, and determines the isotherms. Finally, one employs the Cooper–Frye formula [35] to calculate particle spectra along the isotherm corresponding to the particular freeze-out temperature (for a detailed discussion of this approach see, for instance, [37]). We note that the Cooper–Frye formalism holds rigorously only on space-like hypersurfaces. For time-like hypersurfaces it may yield negative numbers of particles emitted from the hypersurface (corresponding to particles that do not freeze out but reenter the fluid). To cure this obviously unphysical result, modifications have been proposed in [36, 38]. The approach of Ref. [38] is, however, problematic since it does not describe correctly radiation from a static source. When modifying the particle spectra as proposed in [36] we found, however, for the cases under consideration virtually no deviation to the results obtained with the conventional approach of Cooper and Frye. Therefore, we will use this well-established method throughout the following.

The two–particle correlation function measures the coincidence probability $P(\mathbf{p}_1, \mathbf{p}_2)$ of two (identical) particles with momenta $\mathbf{p}_1$, $\mathbf{p}_2$ relative to the probability of detecting uncorrelated particles from different events,

$$C_2(\mathbf{p}_1, \mathbf{p}_2) = \frac{P(\mathbf{p}_1, \mathbf{p}_2)}{P(\mathbf{p}_1) P(\mathbf{p}_2)} \ . \tag{17}$$

In the following, the average 4–momentum is denoted as $K^\mu = (p_1^\mu + p_2^\mu)/2$ and the relative 4–momentum as $q^\mu = p_1^\mu - p_2^\mu$. Under the assumption that the particle source is chaotic and sufficiently large, and that the emitted particles are bosons (with degeneracy factor d) the two–particle correlation function can be written as [34]

$$C_2(\mathbf{p}_1, \mathbf{p}_2) = 1 + \frac{\left| \frac{d}{(2\pi)^3} \int_\Sigma \mathrm{d}\Sigma \cdot K \ \exp\left[i\, \Sigma \cdot q\right] \ f\left(\frac{u \cdot K}{T}\right) \right|^2}{E_1 \frac{\mathrm{d}N}{\mathrm{d}^3\mathbf{p_1}} \ E_2 \frac{\mathrm{d}N}{\mathrm{d}^3\mathbf{p_2}}} \ , \tag{18}$$

where [35]

$$E \frac{\mathrm{d}N}{\mathrm{d}^3\mathbf{p}} = \frac{d}{(2\pi)^3} \int_\Sigma \mathrm{d}\Sigma \cdot p \ f\left(\frac{u \cdot p}{T}\right) \tag{19}$$

is the single inclusive momentum distribution. $f(x) = (e^x - 1)^{-1}$ is the Bose–Einstein distribution function, and u^μ the fluid 4–velocity. The integrals run over the freeze-out hypersurface. In general, that hypersurface is represented by a 3–parametric (4–vector) function $\Sigma^\mu(\zeta, \eta, \phi)$, and the normal vector on the hypersurface is determined by

$$\mathrm{d}\Sigma_\mu = \epsilon_{\mu\alpha\beta\gamma} \frac{\partial \Sigma^\alpha}{\partial \zeta} \frac{\partial \Sigma^\beta}{\partial \eta} \frac{\partial \Sigma^\gamma}{\partial \phi} \, \mathrm{d}\zeta \, \mathrm{d}\eta \, \mathrm{d}\phi \ , \tag{20}$$

where $\epsilon_{\mu\alpha\beta\gamma}$ ($= -1$ for $(\mu\alpha\beta\gamma)$ an even permutation of $(0\,1\,2\,3)$) is the completely antisymmetric 4–tensor. While the (freeze-out) temperature T is (by definition) assumed to be constant along the freeze-out hypersurface, the fluid velocity varies, $u^\mu = u^\mu(\Sigma)$.

For symmetric systems, the number of independent variables which C_2 depends on can be reduced. For the spherically symmetric fireball geometry, the orientation of the average momentum can be chosen arbitrarily, such that C_2 depends only on the modulus of $\mathbf{K}$. Our choice of coordinate system will be such that $\mathbf{K} = (0, 0, K)$. Furthermore, $\mathbf{q}$ can be decomposed into a so-called "out" component $\mathbf{q}_{\rm out} = (0, 0, q_{\rm out})$ parallel to $\mathbf{K}$ and a "side" component $\mathbf{q}_{\rm side}$ orthogonal to $\mathbf{K}$ and $\mathbf{q}_{\rm out}$. Rotational symmetry around the direction of $\mathbf{K}$ allows us to choose $\mathbf{q}_{\rm side} = (q_{\rm side}, 0, 0)$, such that the correlation function depends only on three independent variables, $C_2(K,\, q_{\rm out},\, q_{\rm side})$.

For the Bjorken cylinder geometry, we restrict our consideration to particles emitted at midrapidity, $K^z = q^z = 0$. Rotational symmetry around the z–axis allows us to choose the average transverse momentum as $\mathbf{K}_\perp = (K, 0, 0)$, and consequently, $\mathbf{q}_{\rm out} = (q_{\rm out}, 0, 0)$, $\mathbf{q}_{\rm side} = (0, q_{\rm side}, 0)$. Again, $C_2(K, q_{\rm out}, q_{\rm side})$ is a function of three independent variables only. The explicit evaluation of (18) for the fireball and Bjorken cylinder geometry is referred to Appendices A and B, respectively.

As is well known [21], the width of the correlation function in out–direction is inversely proportional to the duration of particle emission, i.e., to the lifetime of the source. Analogously, the inverse width of the correlation function in side–direction is a measure for the (transverse) size of the source. To be more precise, for fixed average (transverse) momentum K we define side– and out–correlation functions as $C_{2,\,\rm side}(q_{\rm side}) \equiv C_2(K, 0, q_{\rm side})$ and $C_{2,\,\rm out}(q_{\rm out}) \equiv C_2(K, q_{\rm out}, 0)$, respectively. We furthermore define a corresponding inverse width as $R_{\rm side} \equiv 1/q^*_{\rm side}$, where $q^*_{\rm side}$ is determined by $C_{2,\,\rm side}(q^*_{\rm side}) = 1.5$, and analogously for $R_{\rm out}$.

We emphasize that we do not attempt a standard Gaussian fit of the two–particle correlation function, which would relate the inverse widths to the usual radii parameters. First of all, we will be interested only in the generic shape of the correlation functions which is satisfactorily characterized by their inverse widths $R_{\rm side}$, $R_{\rm out}$. Second, the functional form of the correlation functions is not a Gaussian (cf. the explicit formulae in Appendix A and B). The fit procedure would therefore only introduce unnecessary errors. Third, the radii parameters as well as the inverse widths are only *proportional* to the actual (average) size and lifetime of the system. It is well known that hydrodynamical flow affects the radii parameters/widths, and, moreover, that this effect is sensitive to the choice of K [21, 34]. It is therefore tedious (if not impossible) to relate $R_{\rm side}$ and $R_{\rm out}$ to the real source size and lifetime. This holds for our model calculations as well as for the experiment.

We can expect, however, that such effects are either irrelevant or largely cancel out if we consider the ratio $R_{\rm out}/R_{\rm side}$. As can be inferred from the space–time diagrams in Figs. 3–5 and 7–9, while the size of the system is approximately constant, it is the lifetime that varies appreciably, depending on whether the system undergoes a phase transition or not. Thus, $R_{\rm out}/R_{\rm side}$ can be expected to be a good measure for the lifetime of the system. In the following, we choose the particles to be pions with mass $m = 138$ MeV, and as average momentum $K = 300$ MeV. On one hand, this value is well within the typical experimental acceptance. On the other hand, it is large enough to exhibit effects of the prolonged lifetime

in the case of a transition to the QGP [21]. To fix the q–scale in MeV we take $R = 5$ fm as a typical initial radius of the system.

In Fig. 14 we show as an example side– and out–correlation functions corresponding to the hydrodynamical evolution of Fig. 4. In light of the uncertainties in the actual freeze-out temperature, we calculate the correlation functions along isotherms for $T = T_c$, $0.9\,T_c$, as well as $0.7\,T_c$. First of all, one immediately recognizes that in all cases the widths of the correlation functions correspond closely to the space–time structure of the corresponding isotherms. For instance, the exceedingly long lifetime of the system in Fig. 4 (b) is reflected in the comparatively small width of the out–correlation function Fig. 14 (b). On the other hand, the transverse size is about the same in all cases, cf. Figs. 4 (b,d,f), which reflects in nearly identical side–correlation functions in Figs. 14 (a,c,e). Furthermore, with the exception of the case $\Delta T = 0.1\,T_c$, the correlation functions are almost completely insensitive to the freeze-out temperature chosen. This is intuitively clear since the corresponding space–time isotherms differ only marginally for $\Delta T = 0$ and the ideal gas calculation, cf. Figs. 4 (b,f), while there are larger differences in Fig. 4 (d). Note that the results shown in Figs. 14 (a,b,e,f) correspond nicely to those in Fig. 4 of [21], in spite of the fact that the latter calculation employs inhomogeneous initial conditions, a different way to solve the hydrodynamical equations, and a different treatment of the freeze-out[3]. In Fig. 15 we show the correlation functions corresponding to the hydrodynamical evolution of Fig. 9. Again, they adequately characterize the space–time geometry of the source.

Fig. 16 shows the experimentally measurable ratio $R_{\rm out}/R_{\rm side}$ as a function of ϵ_0 for the spherical fireball geometry. Comparing the results with Fig. 11, one observes that this ratio reflects closely the behaviour of the lifetime of the system, independent of details in the equation of state such as the width of the transition region ΔT or the latent heat of the transition (which is proportional to d_Q/d_H). Also, for the case of a first order transition, $\Delta T = 0$, Figs. 16 (a,c), the enhancement in $R_{\rm out}/R_{\rm side}$ over the ideal gas case is a factor of 3 to 7 (for $d_Q/d_H = 3$ to $37/3$) at $\epsilon_0 \sim \epsilon_Q$. In the case of a smooth transition, $\Delta T = 0.1\,T_c$, Figs. 16 (b,d), this is considerably reduced (as expected from Fig. 11), but if the system freezes out at temperatures $T_f \leq 0.7\,T_c$, there is still a factor of 2 enhancement over the ideal gas case.

In Figs. 17, 18 we present the corresponding results for the Bjorken cylinder expansion with $\tau_0 = 0.1\,R$ and $\tau_0 = 1/3\,T_0$, respectively. In all cases we find that the experimentally measurable ratio of correlation widths mirrors closely the dependence of the lifetime on initial conditions in Figs. 12, 13. The most favourable case $R_{\rm out}/R_{\rm side} \sim 3.5$ (for a strong first order transition with a large latent heat, $d_Q/d_H = 37/3$, cf. Fig. 17 (a)), may be reached with initial conditions expected at RHIC energies. At that point the enhancement of this ratio is about a factor of 2 above the ideal gas case and virtually independent of the freeze-out temperature. In the scenario with $\tau_0 = 1/3\,T_0$, Fig. 18 (a), the enhancement is somewhat smaller and is shifted toward higher initial energy densities because the initial pure Bjorken expansion phase starts earlier than in the fixed $\tau_0 = 0.1\,R$ case. For a smooth transition with $\Delta T = 0.1\,T_c$, the maximum ratio is reduced to 2.5 and varies less rapidly with ϵ_0, but is still

[3]The freeze-out in [21] is in some sense performed dynamically, the freeze-out surface, however, is assumed to have no time-like parts.

about 40% larger than for the ideal gas expansion. In this case, however, a significant time delay can only be observed if the freeze-out occurs relatively late with $T_f \sim 0.7\,T_c$. As seen in Figs. 17, 18, for earlier freeze-out, smaller τ_0, or smaller d_Q/d_H the enhancement relative to the ideal gas case is significantly reduced and would be more difficult to observe.

At energy densities estimated to be reached in CERN SPS Pb+Pb–collisions ($\epsilon_0 \sim 1 - 2\,T_c\,s_c$ in our units), we expect from our results that $R_{\rm out}/R_{\rm side} \sim 1.5 - 2$. However, present data from CERN SPS [39] indicate that the (fitted) out–radii are rather similar to the side–radii. This does not contradict our results, because, as shown by Schlei et al. [40] in the framework of a hydrodynamical calculation similar to ours, correlation functions constructed from thermal pions only give $R_{\rm out}/R_{\rm side} \sim 2$ (cf. especially [34]), while the incorporation of long-lived *resonance decays* leads to a reduction of that ratio and good agreement with the measured radii. We note that kaon interferometry [41, 42, 43] is preferable, though experimentally more difficult, because only distortions of the interference pattern due to shorter lived K^* resonances have to be taken into account.

5 Conclusions

In this paper we investigated the spherically symmetric expansion of a fireball as well as the cylindrically symmetric transverse expansion of a QGP with boost-invariant initial conditions along the beam axis. The expansion was treated in the framework of ideal relativistic hydrodynamics and extends our systematic study [13, 14, 16, 31, 37] of collective flow patterns with realistic equations of state. The symmetries of the considered geometries allowed us to calculate the flow patterns using a simple modification of a well-tested one–dimensional algorithm.

The emphasis of the present investigation was on how a rapid cross-over to the QGP in the equation of state influences the collective expansion dynamics. In particular, since present lattice data only constrain the width of the transition region to the QGP to be in the range $0 \leq \Delta T < 0.1\,T_c$, it is important to test how such uncertainties may influence dynamical observables. We also studied the effect of varying the ratio of degrees of freedom in the QGP and hadron phase (i.e. essentially the latent heat of the transition) on the system dynamics. The results were compared to the expansion of an ultrarelativistic ideal gas (without transition) using fixed energy density initial conditions.

We focussed on the lifetime of the system as a function of initial energy density as an important *collective* observable that can discriminate between different equations of state. As expected from previous one–dimensional studies in the framework of the Landau expansion model [14], we found that the lifetime of a spherical fireball is much longer in the case of a first order phase transition, $\Delta T = 0$, as compared to the expansion of an ideal gas without transition. The prolongation of the lifetime in that case can be up to a factor of 4.5 to 9 (for $d_Q/d_H = 3$ to 37/3, respectively), provided the initial energy density corresponds to that of mixed phase with a large fraction of QGP. This time delay effect was originally pointed out by Pratt [21]. In the case of a smooth transition, $\Delta T = 0.1\,T_c$, however, this time delay is drastically reduced. The lifetimes (of matter with $T = 0.7\,T_c$) nevertheless still remain on the order of a factor of 2 longer as compared to the ideal gas expansion.

For the Bjorken cylinder expansion, it is also necessary to specify the initial (proper) time τ_0 for the onset of hydrodynamic expansion. To explore uncertainties associated with this additional degree of freedom, we investigated the cases $\tau_0 = 0.5\,R$, $0.1\,R$, and a dynamical $\tau_0 = 1/3\,T_0$ varying with the initial temperature. The results were similar as for the spherical expansion, up to two important exceptions: (a) the maximum lifetimes emerged at higher initial energy densities (the exact value of which depends on the choice of τ_0) corresponding to QGP matter instead of mixed phase matter, and (b) the lifetimes were in general shorter.

Both effects are explained by the very efficient cooling due to the initial longitudinal velocity profile associated with the boost invariance of the problem. This effect causes an overall reduction of the lifetimes. Moreover, in order for slow (van Hove [19]) deflagration fronts to dominate the cooling mechanism in transverse direction, one has to start at higher initial energy densities to compensate for the longitudinal cooling. Otherwise, the longitudinal cooling reduces the energy densities too fast and the associated deflagration solution [13] vanishes. Further cooling is then achieved (in the usual way) through a (fast) simple wave.

Finally, we showed (cf. also [21, 22]) that the prolongation of the lifetime can be observable via the ratio $R_{\rm out}/R_{\rm side}$ of inverse widths of two–particle correlation functions in out– and side–direction. This ratio follows the behaviour of the lifetimes rather closely. The prolongation of the lifetime in the case of a transition to the QGP could therefore be in principle searched for using this observable. The enhancement of that ratio is, of course, strongest in the case that the transition is first order with a large latent heat. An interesting result is that, for the fireball geometry, the effect is maximum for energy densities achieved at the AGS, while for the Bjorken cylinder geometry, the maximum of $R_{\rm out}/R_{\rm side}$ occurs at energy densities presumably reached at the RHIC collider.

There are several effects which may reduce the strength of the time–delay signal observable via the $R_{\rm out}/R_{\rm side}$–ratios that will require further investigation. First, for the fireball geometry it is important to extend our considerations to finite baryon number density. At finite chemical potential the width of the cross-over region may be significantly larger than at zero chemical potential. Second, the decay of long-lived resonances can simulate time delay [44]. Interferometry with kaons instead of pions is therefore preferable [43]. Finally, while our investigations covered a wide range of uncertainties in the equation of state, our calculations have neglected effects of dissipation that tend in general to reduce the collective flow strengths predicted via ideal hydrodynamics. For instance, bulk viscosity appears in the hydrodynamical equations of motion in a similar way as the pressure, and could in principle counteract any reduction of the velocity of sound in the transition region. The main result of this paper is, nevertheless, that the generic time–delay signature of QGP formation is remarkable robust to present uncertainties in the QCD equation of state.

Acknowledgments

We thank G. Bertsch, A. Dumitru, and E. Shuryak for stimulating discussions on the lifetime of the QGP. One of us (D.H.R.) benefitted considerably from discussions with B. Schlei on the calculation of two–particle correlation functions in the hydrodynamical framework. We thank U. Heinz and W. Zajc for useful discussions on our results and D. Keane for empha-

sizing that kaons might be the ideal probe to detect a prolonged lifetime with the STAR detector at RHIC.

Appendix A

In this Appendix we explicitly calculate the out– and side–correlation functions in the fireball geometry. We first specify the parameters of the freeze-out hypersurface. For the following discussion, we conveniently choose spherical coordinates r, θ, φ in space. Let (a) ζ parametrize the surface in the $t-r$ plane, $0 \leq \zeta \leq 1$, with the lower boundary corresponding to $t = 0$ and the upper to $r = 0$. Let (b) η parametrize the surface in the $r-\theta$ plane and (c) ϕ in the $r-\varphi$ plane. In the $t-r$ plane, the surface is given by the corresponding isotherm shown in Figs. 3–5. Due to spherical symmetry, however, the surface in the $r-\theta$ and $r-\varphi$ planes is trivial. We can simply identify $\eta = \theta$, $\phi = \varphi$ and vary them within the standard boundaries for the azimuthal and polar angle. As a consequence, the time t_f and the radius r_f at freeze-out depend only on ζ, not on η or ϕ. The freeze-out surface is thus given by $\Sigma^\mu = (t_f(\zeta), r_f(\zeta)\,\mathbf{e}_r)$, where $\mathbf{e}_r = (\sin\eta\,\cos\phi, \sin\eta\,\sin\phi, \cos\eta)$.

Applying (20) and choosing the sign to have $\mathrm{d}\Sigma_\mu$ pointing outwards along the isotherm, we obtain

$$\mathrm{d}\Sigma_\mu = \left(-\frac{\mathrm{d}r_f}{\mathrm{d}\zeta}, \frac{\mathrm{d}t_f}{\mathrm{d}\zeta}\,\mathbf{e}_r\right) r_f^2(\zeta)\,\sin\eta\;\mathrm{d}\zeta\,\mathrm{d}\eta\,\mathrm{d}\phi\;. \tag{21}$$

For the calculation of the correlation function we employ the Boltzmann approximation. For an average momentum $K = 300$ MeV chosen in our calculations the error introduced is negligible, in particular since we also consider the particles to be massive pions, $m = 138$ MeV, and choose $T_c = 160$ MeV.

For the single inclusive pion spectrum (19), one conveniently chooses $\mathbf{p} = (0, 0, p)$, and obtains after inserting (21) and performing the ϕ– and η–integrations

$$E\,\frac{\mathrm{d}N}{\mathrm{d}^3\mathbf{p}} = \frac{d}{2\pi^2}\int_0^1 \mathrm{d}\zeta\; r_f^2(\zeta)\,e^{-E\gamma/T}\left\{-E\,\frac{\sinh a}{a}\;\frac{\mathrm{d}r_f}{\mathrm{d}\zeta} + p\left[\frac{\cosh a}{a} - \frac{\sinh a}{a^2}\right]\frac{\mathrm{d}t_f}{\mathrm{d}\zeta}\right\}\;, \tag{22}$$

where $a \equiv pv\gamma/T$, $E = [\mathbf{p}^2 + m^2]^{1/2}$, and v is the (radial) fluid 3–velocity, $\gamma = [1 - v^2]^{-1/2}$. Here (and in the following), the ζ–integration has to be done numerically along the respective isotherms obtained from the solution of the hydrodynamical equations. For further use, we define

$$\mathcal{I}_0(p) \equiv \frac{(2\pi)^3}{d}\,E\,\frac{\mathrm{d}N}{\mathrm{d}^3\mathbf{p}}\;. \tag{23}$$

For the side–correlation function, $q_{\mathrm{out}} = 0$, and consequently

$$p_1^\mu = (E, q_{\mathrm{side}}/2, 0, K)\;, \tag{24}$$

$$p_2^\mu = (E, -q_{\mathrm{side}}/2, 0, K)\;, \tag{25}$$

$$K^\mu = (E, 0, 0, K)\;, \tag{26}$$

$$q^\mu = (0, q_{\mathrm{side}}, 0, 0)\;, \tag{27}$$

where $E = [K^2 + q_{\mathrm{side}}^2/4 + m^2]^{1/2}$. Since the single inclusive spectrum (22) does not depend on the direction of $\mathbf{p}$, the two single inclusive spectra in the denominator in (18) are equal. Furthermore, for the numerator one has to calculate the expressions

$$\mathcal{I}_1 \equiv \int_\Sigma \mathrm{d}\Sigma\cdot K\,e^{-u\cdot K/T}\,\cos\left[\Sigma\cdot q\right]\;, \tag{28}$$

$$\mathcal{I}_2 \;\equiv\; \int_\Sigma \mathrm{d}\Sigma \cdot K\, e^{-u\cdot K/T}\, \sin\left[\Sigma\cdot q\right] \,. \tag{29}$$

For the calculation of $\mathcal{I}_1$ we insert (21) and perform the ϕ–integration with the help of eq. (3.715.18) of Ref. [45]. Subsequently, the η–integration can be done with an analytic continuation of either eq. (6.616.5) or (6.677.6) of [45] and a suitable first derivative of these formulae. The final result reads

$$\begin{aligned}\mathcal{I}_1 \;&=\; 4\pi \int_0^1 \mathrm{d}\zeta\, r_f^2(\zeta)\, e^{-E\gamma/T} \qquad (30)\\ &\times\; \left\{-E\,\frac{\sinh\sqrt{a^2-b^2}}{\sqrt{a^2-b^2}}\,\frac{\mathrm{d}r_f}{\mathrm{d}\zeta} + K\,\frac{a}{\sqrt{a^2-b^2}}\left[\frac{\cosh\sqrt{a^2-b^2}}{\sqrt{a^2-b^2}} - \frac{\sinh\sqrt{a^2-b^2}}{a^2-b^2}\right]\frac{\mathrm{d}t_f}{\mathrm{d}\zeta}\right\}\,,\end{aligned}$$

where $a \equiv Kv\gamma/T$, $b \equiv q_{\mathrm{side}}\, r_f$. It is easy to show that for the side–correlation function, $\mathcal{I}_2 \equiv 0$ by symmetry. The final result thus reads

$$C_{2,\,\mathrm{side}} = 1 + \mathcal{I}_1^2/\mathcal{I}_0^2 \,, \tag{31}$$

with $\mathcal{I}_0$ from (23) and $\mathcal{I}_1$ from (30).

For the out–correlation function, $q_{\mathrm{side}} = 0$, and consequently

$$\begin{aligned} p_1^\mu \;&=\; (E_1, 0, 0, K + q_{\mathrm{out}}/2) \,, &(32)\\ p_2^\mu \;&=\; (E_2, 0, 0, K - q_{\mathrm{out}}/2) \,, &(33)\\ K^\mu \;&=\; (K^0, 0, 0, K) \,, &(34)\\ q^\mu \;&=\; (E_1 - E_2, 0, 0, q_{\mathrm{out}}) \,, &(35)\end{aligned}$$

where $E_{1,2} = [(K \pm q_{\mathrm{out}}/2)^2 + m^2]^{1/2}$, $K^0 = (E_1 + E_2)/2$. The ϕ–integration in the calculation of $\mathcal{I}_1$, $\mathcal{I}_2$ is now trivial. For the η–integration, we employ the angle addition theorem and eqs. (2.662.1,2) of [45], obtaining

$$\begin{aligned}\mathcal{I}_1 \;&=\; 4\pi \int_0^1 \mathrm{d}\zeta\, r_f^2(\zeta)\, e^{-K^0\gamma/T} \left\{-K^0\,\left[\cos\beta\,\mathcal{J}_0(a,b) + \sin\beta\,\mathcal{J}_1(a,b)\right]\,\frac{\mathrm{d}r_f}{\mathrm{d}\zeta}\right.\\ &\left. + K\left[\cos\beta\,\frac{\partial\mathcal{J}_0(a,b)}{\partial a} + \sin\beta\,\frac{\partial\mathcal{J}_1(a,b)}{\partial a}\right]\frac{\mathrm{d}t_f}{\mathrm{d}\zeta}\right\}\,, \qquad (36)\end{aligned}$$

where $\beta \equiv (E_1 - E_2)t_f$, and

$$\mathcal{J}_0(a,b) \equiv \frac{a\,\cos b\,\sinh a + b\,\sin b\,\cosh a}{a^2+b^2}\;,\quad \mathcal{J}_1(a,b) \equiv \frac{a\,\sin b\,\cosh a - b\,\cos b\,\sinh a}{a^2+b^2}\;, \tag{37}$$

with $a \equiv Kv\gamma/T$ and $b \equiv q_{\mathrm{out}}\, r_f$. In complete analogy one obtains $\mathcal{I}_2$ as

$$\begin{aligned}\mathcal{I}_2 \;&=\; 4\pi \int_0^1 \mathrm{d}\zeta\, r_f^2(\zeta)\, e^{-K^0\gamma/T} \left\{-K^0\,\left[\sin\beta\,\mathcal{J}_0(a,b) - \cos\beta\,\mathcal{J}_1(a,b)\right]\,\frac{\mathrm{d}r_f}{\mathrm{d}\zeta}\right.\\ &\left. + K\left[\sin\beta\,\frac{\partial\mathcal{J}_0(a,b)}{\partial a} - \cos\beta\,\frac{\partial\mathcal{J}_1(a,b)}{\partial a}\right]\frac{\mathrm{d}t_f}{\mathrm{d}\zeta}\right\}\,. \qquad (38)\end{aligned}$$

Finally, the out–correlation function reads

$$C_{2,\,\mathrm{out}} = 1 + \frac{\mathcal{I}_1^2 + \mathcal{I}_2^2}{\mathcal{I}_0(p_1)\;\mathcal{I}_0(p_2)} \,. \tag{39}$$

Appendix B

In this Appendix we explicitly calculate the out– and side–correlation functions in the Bjorken cylinder geometry. Convenient coordinates to work in are cylindrical coordinates r, φ, z in space. As in the preceding Appendix, (a) ζ parametrizes the freeze-out surface in the $t-r$ plane (at $z=0$), $0 \le \zeta \le 1$, $t_f(0)=\tau_0$, $r_f(1)=0$. (b) η parametrizes the surface in the $t-z$ plane. Due to boost invariance, that surface is simply the space–time hyperbola of constant $\tau_f = \sqrt{t_f^2 - z_f^2}$. Note that at $z=0$, $\tau_f = t_f(\zeta)$ and therefore τ_f depends on ζ. A natural choice for the parameter η is the space–time rapidity $\mathrm{Artanh}\,[z_f/t_f]$ (as implied by our choice of symbols), such that $t_f(\zeta,\eta) = \tau_f(\zeta)\,\cosh\eta$, $z_f(\zeta,\eta) = \tau_f(\zeta)\,\sinh\eta$. Finally, (c) ϕ parametrizes the hypersurface in the $r-\varphi$ plane and due to cylindrical symmetry can be identified with the polar angle, $\phi \equiv \varphi$. We note that due to boost invariance along z, r_f cannot depend on η.

The hypersurface 4–vector thus reads

$$\Sigma^\mu = (\tau_f(\zeta)\,\cosh\eta,\, r_f(\zeta)\,\cos\phi,\, r_f(\zeta)\,\sin\phi,\, \tau_f(\zeta)\,\sinh\eta)\ , \tag{40}$$

with $\tau_f(\zeta) \equiv t_f(\zeta,\eta=0)$, i.e., given by the isotherms in Figs. 7–9. The normal vector (with proper orientation) is readily calculated with (20),

$$\mathrm{d}\Sigma_\mu = \left(-\frac{\mathrm{d}r_f}{\mathrm{d}\zeta}\,\cosh\eta,\, \frac{\mathrm{d}\tau_f}{\mathrm{d}\zeta}\,\cos\phi,\, \frac{\mathrm{d}\tau_f}{\mathrm{d}\zeta}\,\sin\phi,\, \frac{\mathrm{d}r_f}{\mathrm{d}\zeta}\,\sinh\eta\right) r_f(\zeta)\,\tau_f(\zeta)\,\mathrm{d}\zeta\,\mathrm{d}\eta\,\mathrm{d}\phi\ . \tag{41}$$

For the calculation of the single inclusive spectrum, we employ $m_\perp \equiv [\mathbf{p}_\perp^2 + m^2]^{1/2}$, i.e., $p^0 = m_\perp\,\cosh y$, $p^z = m_\perp\,\sinh y$, with the longitudinal (particle) rapidity $y \equiv \mathrm{Artanh}\,[p^z/E]$. Furthermore, due to rotational symmetry around z, we may choose $\mathbf{p}_\perp = (p_\perp, 0, 0)$. Thus,

$$\mathrm{d}\Sigma\cdot p = \left(-m_\perp\cosh\left[y-\eta\right]\frac{\mathrm{d}r_f}{\mathrm{d}\zeta} + p_\perp\cos\phi\,\frac{\mathrm{d}\tau_f}{\mathrm{d}\zeta}\right) r_f(\zeta)\,\tau_f(\zeta)\,\mathrm{d}\zeta\,\mathrm{d}\eta\,\mathrm{d}\phi\ . \tag{42}$$

The fluid 4–velocity in the Bjorken cylinder expansion reads $u^\mu = \gamma\,(1,\, v\,\mathbf{e}_r,\, z/t)$, where $v \equiv v_\perp$, $\mathbf{e}_r = (\cos\phi, \sin\phi, 0)$. With the (longitudinal) space–time rapidity $\eta \equiv \mathrm{Artanh}\,[z/t]$ and the transverse fluid rapidity $\eta_r \equiv \mathrm{Artanh}\,[v\,\cosh\eta]$, one obtains

$$u^\mu = (\cosh\eta\,\cosh\eta_r,\, \sinh\eta_r\,\mathbf{e}_r,\, \sinh\eta\,\cosh\eta_r)\ . \tag{43}$$

Note that longitudinal boost invariance implies that η_r cannot depend on η, and is therefore given by the solution of the hydrodynamical equations at $z=0$, $\eta_r \equiv \mathrm{Artanh}\,[v(z=0)]$, as provided in Section 3.

For the single inclusive momentum distribution (in Boltzmann approximation) we insert (42) and (43) into (19), perform the η–integration with the help of eq. (3.547.4) of [45], and the ϕ–integration using the formula (3.937.2) [45], resulting in

$$\begin{aligned} E\,\frac{\mathrm{d}N}{\mathrm{d}^3\mathbf{p}} \;=\; & \frac{d}{2\pi^2}\int_0^1 \mathrm{d}\zeta\, r_f(\zeta)\,\tau_f(\zeta)\left\{-m_\perp\,K_1\left(\frac{m_\perp\cosh\eta_r}{T}\right) I_0\left(\frac{p_\perp\sinh\eta_r}{T}\right)\frac{\mathrm{d}r_f}{\mathrm{d}\zeta}\right. \\ & \left. + p_\perp\,K_0\left(\frac{m_\perp\cosh\eta_r}{T}\right) I_1\left(\frac{p_\perp\sinh\eta_r}{T}\right)\frac{\mathrm{d}\tau_f}{\mathrm{d}\zeta}\right\}\ . \end{aligned} \tag{44}$$

Note that the final spectrum respects the symmetries of the problem, i.e., it is azimuthally symmetric and boost invariant along z. For further use, let us define

$$\mathcal{I}_0(p_\perp) = \frac{(2\pi)^3}{d}\, E\, \frac{\mathrm{d}N}{\mathrm{d}^3\mathbf{p}} \ . \tag{45}$$

For the side–correlation function for particles at $y = 0$ we may choose $\mathbf{K}_\perp = (K, 0, 0)$ such that

$$\begin{aligned} p_1^\mu &= (E, K, q_{\mathrm{side}}/2, 0) \ , & (46)\\ p_2^\mu &= (E, K, -q_{\mathrm{side}}/2, 0) \ , & (47)\\ K^\mu &= (E, K, 0, 0) \ , & (48)\\ q^\mu &= (0, 0, q_{\mathrm{side}}, 0) \ , & (49) \end{aligned}$$

where $E = [K^2 + q_{\mathrm{side}}^2/4 + m^2]^{1/2}$. As in the previous case of the fireball geometry (Appendix A), one has to calculate $\mathcal{I}_1$ and $\mathcal{I}_2$. While the latter vanishes again by symmetry, the former reads after using eq. (3.547.4) of [45] in the η–integration

$$\begin{aligned} \mathcal{I}_1 \ = \ 4\pi \int_0^1 \mathrm{d}\zeta\, r_f(\zeta)\, \tau_f(\zeta) \Bigg\{ & -E\, K_1\left(\frac{E\cosh\eta_r}{T}\right) \hat{I}_0(a,b)\, \frac{\mathrm{d}r_f}{\mathrm{d}\zeta} \\ & + K\, K_0\left(\frac{E\cosh\eta_r}{T}\right) \hat{I}_1(a,b)\, \frac{\mathrm{d}\tau_f}{\mathrm{d}\zeta} \Bigg\} \ , \end{aligned} \tag{50}$$

where $a \equiv K \sinh\eta_r/T$, $b \equiv q_{\mathrm{side}}\, r_f$, and the functions $\hat{I}_0$, $\hat{I}_1$ (which have to be evaluated numerically) are defined by

$$\begin{aligned} \hat{I}_0(a,b) \ &\equiv \ \frac{1}{\pi}\int_0^\pi \mathrm{d}\phi\, \cosh\left[a\,\cos\phi\right]\, \cos\left[b\,\sin\phi\right] \ , & (51)\\ \hat{I}_1(a,b) \ &\equiv \ \frac{1}{\pi}\int_0^\pi \mathrm{d}\phi\, \cos\phi\, \sinh\left[a\,\cos\phi\right]\, \cos\left[b\,\sin\phi\right] \equiv \frac{\partial \hat{I}_0(a,b)}{\partial a} \ . & (52) \end{aligned}$$

It is obvious (see eqs. (8.411.1, 8.431.4) in [45]) that $\hat{I}_0$ is related to the Bessel functions I_0, J_0:

$$\hat{I}_0(a,0) = I_0(a) \ , \quad \hat{I}_0(0,b) = J_0(b) \ . \tag{53}$$

The final result for the side–correlation function reads (as in the preceding Appendix)

$$C_{2,\,\mathrm{side}} = 1 + \mathcal{I}_1^2/\mathcal{I}_0^2 \ , \tag{54}$$

with $\mathcal{I}_1$ from (50) and $\mathcal{I}_0$ from (45) with the single inclusive spectrum (44).

For the out–correlation the choice of momenta is

$$\begin{aligned} p_1^\mu &= (E_1, K + q_{\mathrm{out}}/2, 0, 0) \ , & (55)\\ p_2^\mu &= (E_2, K - q_{\mathrm{out}}/2, 0, 0) \ , & (56)\\ K^\mu &= (K^0, K, 0, 0) \ , & (57)\\ q^\mu &= (E_1 - E_2, q_{\mathrm{out}}, 0, 0) \ , & (58) \end{aligned}$$

where $E_{1,2} = [(K \pm q_{\rm out}/2)^2 + m^2]^{1/2}$, $K^0 = (E_1 + E_2)/2$. As in the previous cases, the η– and ϕ–integrations separate, and the final result for $\mathcal{I}_1$ and $\mathcal{I}_2$ reads

$$\begin{aligned}
\mathcal{I}_1 &= 4\pi \int_0^1 {\rm d}\zeta\, r_f(\zeta)\, \tau_f(\zeta) \Big\{ -K^0 \left[\mathcal{K}_1(\alpha,\beta)\, \mathcal{J}_0(a,b) + \hat{\mathcal{K}}_1(\alpha,\beta)\, \hat{\mathcal{J}}_0(a,b) \right] \frac{{\rm d}r_f}{{\rm d}\zeta} \\
&\qquad + K \left[\mathcal{K}_0(\alpha,\beta)\, \mathcal{J}_1(a,b) + \hat{\mathcal{K}}_0(\alpha,\beta)\, \hat{\mathcal{J}}_1(a,b) \right] \frac{{\rm d}\tau_f}{{\rm d}\zeta} \Big\} \ , \quad (59) \\
\mathcal{I}_2 &= 4\pi \int_0^1 {\rm d}\zeta\, r_f(\zeta)\, \tau_f(\zeta) \Big\{ -K^0 \left[\hat{\mathcal{K}}_1(\alpha,\beta)\, \mathcal{J}_0(a,b) - \mathcal{K}_1(\alpha,\beta)\, \hat{\mathcal{J}}_0(a,b) \right] \frac{{\rm d}r_f}{{\rm d}\zeta} \\
&\qquad + K \left[\hat{\mathcal{K}}_0(\alpha,\beta)\, \mathcal{J}_1(a,b) - \mathcal{K}_0(\alpha,\beta)\, \hat{\mathcal{J}}_1(a,b) \right] \frac{{\rm d}\tau_f}{{\rm d}\zeta} \Big\} \ , \quad (60)
\end{aligned}$$

where $\alpha \equiv K^0 \cosh\eta_r/T$, $\beta \equiv (E_1 - E_2)\tau_f$, $a \equiv K \sinh\eta_r/T$, $b \equiv q_{\rm out}\, r_f$, and (see eqs. (8.431.4, 8.431.5, 8.432.1, 8.476.4) in [45])

$$\begin{aligned}
\mathcal{K}_0(\alpha,\beta) &\equiv \int_0^\infty {\rm d}\eta\, \cos\left[\beta\, \cosh\eta\right] e^{-\alpha\, \cosh\eta} \equiv {\rm Re}\, K_0(\alpha - i\beta) \ , \quad (61) \\
\mathcal{K}_1(\alpha,\beta) &\equiv \int_0^\infty {\rm d}\eta\, \cosh\eta\, \cos\left[\beta\, \cosh\eta\right] e^{-\alpha\, \cosh\eta} \equiv {\rm Re}\, K_1(\alpha - i\beta) \equiv -\frac{\partial \mathcal{K}_0(\alpha,\beta)}{\partial\alpha} \ , \quad (62) \\
\hat{\mathcal{K}}_0(\alpha,\beta) &\equiv \int_0^\infty {\rm d}\eta\, \sin\left[\beta\, \cosh\eta\right] e^{-\alpha\, \cosh\eta} \equiv {\rm Im}\, K_0(\alpha - i\beta) \ , \quad (63) \\
\hat{\mathcal{K}}_1(\alpha,\beta) &\equiv \int_0^\infty {\rm d}\eta\, \cosh\eta\, \sin\left[\beta\, \cosh\eta\right] e^{-\alpha\, \cosh\eta} \equiv {\rm Im}\, K_1(\alpha - i\beta) \equiv -\frac{\partial \hat{\mathcal{K}}_0(\alpha,\beta)}{\partial\alpha} \ , \quad (64) \\
\mathcal{J}_0(a,b) &\equiv \frac{1}{\pi} \int_0^\pi {\rm d}\phi\, \cos\left[b \cos\phi\right]\, \cosh\left[a\, \cos\phi\right] \equiv {\rm Re}\, I_0(a + ib) \ , \quad (65) \\
\mathcal{J}_1(a,b) &\equiv \frac{1}{\pi} \int_0^\pi {\rm d}\phi\, \cos\phi\, \cos\left[b \cos\phi\right]\, \sinh\left[a\, \cos\phi\right] \equiv {\rm Re}\, I_1(a + ib) \equiv \frac{\partial \mathcal{J}_0(a,b)}{\partial a} \ , \quad (66) \\
\hat{\mathcal{J}}_0(a,b) &\equiv \frac{1}{\pi} \int_0^\pi {\rm d}\phi\, \sin\left[b \cos\phi\right]\, \sinh\left[a\, \cos\phi\right] \equiv {\rm Im}\, I_0(a + ib) \ , \quad (67) \\
\hat{\mathcal{J}}_1(a,b) &\equiv \frac{1}{\pi} \int_0^\pi {\rm d}\phi\, \cos\phi\, \sin\left[b \cos\phi\right]\, \cosh\left[a\, \cos\phi\right] \equiv {\rm Im}\, I_1(a + ib) \equiv \frac{\partial \hat{\mathcal{J}}_0(a,b)}{\partial a} \ . \quad (68)
\end{aligned}$$

The final result for the out–correlation reads

$$C_{2,\,\rm out} = 1 + \frac{\mathcal{I}_1^2 + \mathcal{I}_2^2}{\mathcal{I}_0(p_{1,\perp})\ \mathcal{I}_0(p_{2,\perp})} \ , \quad (69)$$

as before, cf. (39), but with $\mathcal{I}_1, \mathcal{I}_2$ from (59) and (60) and $\mathcal{I}_0$ from (45) with the single inclusive spectrum (44).

References

[1] E. Laermann, Proc. of "Quark Matter '96", May 20 – 24, 1996, Heidelberg, Germany (to appear in Nuclear Physics A).

[2] see, for instance:
S.A. Chin, Phys. Lett. B 119 (1982) 51,
L.D. McLerran and T. Toimela, Phys. Rev. D 31 (1985) 545,
R.C. Hwa and K. Kajantie, Phys. Rev. D 32 (1985) 1109,
K. Kajantie, J. Kapusta, L. McLerran, A. Mekjian, Phys. Rev. D 34 (1986) 2746.

[3] T. Matsui and H. Satz, Phys. Lett. B 178 (1986) 416.

[4] M. Gyulassy and M. Plümer, Phys. Lett. B 243 (1990) 432.

[5] C. Greiner, D.H. Rischke, H. Stöcker, P. Koch, Phys. Rev. D 38 (1988) 2797.

[6] K. Rajagopal, F. Wilczek, Nucl. Phys. B 399 (1993) 395.

[7] J. Kapusta, P. Lichard, D. Seibert, Phys. Rev. D 44 (1991) 2774.

[8] M. Gonin, Proc. of "Quark Matter '96", May 20 – 24, 1996, Heidelberg, Germany (to appear in Nucl. Phys. A).

[9] C. Gerschel and J. Hüfner, Nucl. Phys. A 544 (1992) 513c.

[10] For a review, see: R.B. Clare and D.D. Strottman, Phys. Rep. 141 (1986) 177.

[11] X.-N. Wang, M. Gyulassy, M. Plümer, Phys. Rev. D 51 (1995) 3436,
R. Baier, Yu.L. Dokshitzer, S. Peigné, D. Schiff, Phys. Lett. B 345 (1995) 277,
R. Baier, Yu.L. Dokshitzer, A.H. Mueller, S. Peigné, D. Schiff, preprint CERN–TH–96/14, 1996 (unpublished).

[12] C.M. Hung and E.V. Shuryak, Phys. Rev. Lett. 75 (1995) 4003.

[13] D.H. Rischke, S. Bernard, J.A. Maruhn, Nucl. Phys. A 595 (1995) 346.

[14] D.H. Rischke and M. Gyulassy, Nucl. Phys. A 597 (1996) 701.

[15] L.V. Bravina, N.S. Amelin, L.P. Csernai, P. Levai, D. Strottman, Nucl. Phys. A 566 (1994) 461c.

[16] D.H. Rischke, Y. Pürsün, J.A. Maruhn, H. Stöcker, W. Greiner, preprint CU–TP–695, nucl–th/9505014, to be published in Heavy Ion Phys.

[17] J. Barrette et al. (E877 collaboration), Phys. Rev. Lett. 73 (1994) 2532, Nucl. Phys. A 590 (1995) 259c,
Y. Zhang and J.P. Wessels (E877 collaboration), Nucl. Phys. A 590 (1995) 557c,
G. Rai and the E895 collaboration, LBL PUB–5399 (1993).

[18] L.D. Landau, Izv. Akd. Nauk SSSR 17 (1953) 51, in: "Collected papers of L.D. Landau" (ed. D. Ter–Haar, Pergamon, Oxford, 1965), p. 569–585,
L.D. Landau and S.Z. Belenkii, Uspekhi Fiz. Nauk 56 (1955) 309, in: "Collected papers of L.D. Landau" (ed. D. Ter–Haar, Pergamon, Oxford, 1965), p. 665–700.

[19] L. Van Hove, Z. Phys. C 21 (1983) 93,
M. Gyulassy, K. Kajantie, H. Kurki–Suonio, L. McLerran, Nucl. Phys. B 237 (1984) 477.

[20] J.D. Bjorken, Phys. Rev. D 27 (1983) 140.

[21] S. Pratt, Phys. Rev. C 49 (1994) 2722, Phys. Rev. D 33 (1986) 1314.

[22] G. Bertsch, M. Gong, M. Tohyama, Phys. Rev. C 37 (1988) 1896,
G. Bertsch, Nucl. Phys. A 498 (1989) 173c.

[23] J.P. Blaizot and J.Y. Ollitrault, Phys. Rev. D 36 (1987) 916.

[24] A. Chodos, R.L. Jaffe, K. Johnson, C.B. Thorn, V.F. Weisskopf, Phys. Rev. D 9 (1974) 3471.

[25] J.J. Neumann, D. Seibert, G. Fai, Phys. Rev. C 51 (1995) 1460.

[26] E. Shuryak, Phys. Rev. Lett. 68 (1992) 3270,
K.J. Eskola and M. Gyulassy, Phys. Rev. C 47 (1993) 2329.

[27] L.D. Landau and E.M. Lifshitz, "Fluid mechanics" (Pergamon, New York, 1959).

[28] G. Baym, B.L. Friman, J.P. Blaizot, M. Soyeur, W. Czyż, Nucl. Phys. A 407 (1983) 541.

[29] G.A. Sod, J. Fluid Mech. 83 (1977) 785.

[30] V. Schneider et al., J. Comput. Phys. 105 (1993) 92.

[31] D.H. Rischke, Y. Pürsün, J.A. Maruhn, Nucl. Phys. A 595 (1995) 383.

[32] K. Kajantie, M. Kataja, L. McLerran, P.V. Ruuskanen, Phys. Rev. D 34 (1986) 811,
M. Kataja, P.V. Ruuskanen, L.D. McLerran, H. v. Gersdorff, Phys. Rev. D 34 (1986) 2755.

[33] Yu.M. Sinyukov, Nucl. Phys. A 498 (1989) 151c.

[34] B.R. Schlei, U. Ornik, M. Plümer, R.M. Weiner, Phys. Lett. B 293 (1992) 275.

[35] F. Cooper and G. Frye, Phys. Rev. D 10 (1974) 186,
F. Cooper, G. Frye, E. Schonberg, Phys. Rev. D 11 (1975) 192.

[36] K.A. Bugaev, preprint University Hannover, 1996 (to be published in Nucl. Phys. A).

[37] S. Bernard, J.A. Maruhn, W. Greiner, D.H. Rischke, Nucl. Phys. A (in press).

[38] Yu.M. Sinyukov, Z. Phys. C 43 (1989) 401.

[39] B.V. Jacak (NA44 collaboration), Nucl. Phys. A 590 (1995) 215c.

[40] J. Bolz, U. Ornik, M. Plümer, B.R. Schlei, R.M. Weiner, Phys. Rev. D 47 (1993) 3860, B. Schlei, U. Ornik, M. Plümer, D. Strottman, R.M. Weiner, Los Alamos preprint hep-ph/9509426.

[41] M. Gyulassy and S.S. Padula, Phys. Rev. C 41 (1990) 21.

[42] B.R. Schlei, Los Alamos preprint nucl-th/9605016.

[43] S. Bernard, D.H. Rischke, M. Gyulassy, in preparation.

[44] S.S. Padula and M. Gyulassy, Nucl. Phys. A 544 (1992) 537c.

[45] I.S. Gradsteyn and I.M. Ryzhik, "Table of Integrals, Series, and Products", Academic Press, San Diego, 1980.

Figure Captions:

Fig. 1: (a) the entropy density divided by T^3 (in units of s_c/T_c^3), (b) the energy density divided by T^4 (in units of $T_c\, s_c/T_c^4$) as functions of temperature (in units of T_c), (c) the pressure (in units of $T_c\, s_c$), (d) the square of the velocity of sound as functions of energy density (in units of $T_c\, s_c$). The solid lines correspond to $\Delta T = 0$, the dotted curves to $\Delta T = 0.1\, T_c$. Quantities for the ideal gas equation of state (with d_H degrees of freedom) are represented by dashed lines. The ratio of degrees of freedom in the QGP to those in the hadronic phase is $d_Q/d_H = 37/3$. The critical enthalpy density is $T_c\, s_c \simeq 0.75$ GeV fm^{-3} for the case $d_Q = 37$, $d_H = 3$.

Fig. 2: The expansion of (a,b) a fireball and (c,d) a Bjorken cylinder (with initial time $\tau_0 = 0.1\, R$) for an ideal gas equation of state $p = \epsilon/3$. (a,c) temperature (in units of the initial temperature T_0), (b,d) laboratory energy density (in units of the initial pressure p_0) as functions of radial distance r from the origin (in units of the initial radius R of the system). The profiles are for times $t = \tau_0 + n\lambda R$, $n = 0, 1, 2, ..., 5$, $\lambda = 0.99$. Solid lines are obtained via the semi-analytical method of characteristics [28], dotted curves are produced with the relativistic HLLE algorithm modified with Sod's operator splitting method.

Fig. 3: (a,c,e) temperature profiles for the fireball expansion for times $t = 0.4\, n\lambda R$, $n = 0, 1, ..., 8$ and an initial energy density $\epsilon_0 = \frac{3}{2}\, T_c\, s_c/\,(d_Q/d_H + 1) = 0.1125\, T_c\, s_c \equiv \epsilon_H$. The profiles are alternatingly shown as full and dotted lines in order to better distinguish them. (b,d,f) show isotherms in the corresponding space–time diagrams. The isotherms are labelled with the corresponding temperatures in units of T_c. Figs. (a,b) are calculated with $\Delta T = 0$, (c,d) with $\Delta T = 0.1\, T_c$, and (e,f) with the ideal gas equation of state.

Fig. 4: Same as in Fig. 3, for $\epsilon_0 = 1.875\, T_c\, s_c \sim \epsilon_Q$. Profiles in (a) are for times $t = 2\, n\lambda R$, in (c) for $t = n\lambda R$, and in (e) for $t = 0.5\, n\lambda R$, $n = 0, 1, ..., 10$.

Fig. 5: Same as in Fig. 3, for $\epsilon_0 = 18.75\, T_c\, s_c \sim 10\, \epsilon_Q$. Profiles in (a,c,e) are for times $t = 0.6\, n\lambda R$, $n = 0, 1, ..., 10$.

Fig. 6: Purely longitudinal expansion in the Bjorken model for an initial energy density $\epsilon_0 = 10\, T_c\, s_c$. (a) energy density (in units of $T_c\, s_c$), (b) entropy density (in units of s_c), (c) pressure (in units of $T_c\, s_c$), (d) temperature (in units of T_c) as functions of (proper) time τ (in units of τ_0). Solid lines are for $\Delta T = 0$, dotted for $\Delta T = 0.1\, T_c$, dashed for the ideal gas. Different cooling laws τ^α are indicated.

Fig. 7: Same as in Fig. 3, but for the Bjorken cylinder expansion with $\tau_0 = 0.1\, R$. Profiles in (a,c,e) are for times $t = \tau_0 + 0.1\, n\lambda R$, $n = 0, 1, ..., 8$.

Fig. 8: Same as in Fig. 7, for an initial energy density $\epsilon_0 = 1.875\, T_c\, s_c \sim \epsilon_Q$. Profiles in (a,c,e) are for times $t = \tau_0 + 0.3\, n\lambda R$, $n = 0, 1, ..., 10$.

Fig. 9: Same as in Fig. 7, for an initial energy density $\epsilon_0 = 18.75\, T_c\, s_c \sim 10\, \epsilon_Q$. Profiles in (a,c,e) are for times $t = \tau_0 + 0.6\, n\lambda R$, $n = 0, 1, ..., 10$.

Fig. 10: Lifetimes (in units of the initial radius R of the system) in the one–dimensional (Landau) expansion (cf. also [14]) as a function of the initial energy density (in units of $T_c\, s_c$). (a,b) are for $d_Q/d_H = 37/3$, (c,d) for $d_Q/d_H = 3$. The thick lines in (a,c) are for $\Delta T = 0$, in (b,d) for $\Delta T = 0.1\, T_c$. Thin lines correspond to the ideal gas case. Solid lines are for $T = 0.7\, T_c$, dotted for $\Delta T = 0.9\, T_c$, dashed for $T = T_c$.

Fig. 11: The same as in Fig. 10, but for the fireball expansion.

Fig. 12: The same as in Fig. 10, but for the Bjorken cylinder expansion with $\tau_0 = 0.1\, R$.

Fig. 13: The same as in Fig. 12, but for $\tau_0 = 1/3\, T_0$.

Fig. 14: Two–pion correlation functions in (a,c,e) side– and (b,d,f) out–direction for the fireball expansion with $\epsilon_0 = 1.875\, T_c\, s_c$. The average pion momentum is $K = 300$ MeV, the initial radius R was fixed to be 5 fm. The critical temperature was taken as $T_c = 160$ MeV, the pion mass is $m = 138$ MeV. (a,b) are for $\Delta T = 0$, (c,d) for $\Delta T = 0.1\, T_c$, (e,f) for the ideal gas. Solid, dotted, and dashed lines are the correlation functions as calculated along the $T = 0.7\, T_c$, $0.9\, T_c$, and T_c isotherm, respectively.

Fig. 15: The same as in Fig. 14, but for the Bjorken cylinder expansion with $\tau_0 = 0.1\, R$ and $\epsilon_0 = 18.75\, T_c\, s_c$. The average transverse pion momentum is $K = 300$ MeV, the longitudinal momenta of the pions vanish.

Fig. 16: The same as in Fig. 11, but for the ratio $R_{\rm out}/R_{\rm side}$.

Fig. 17: The same as in Fig. 12, but for the ratio $R_{\rm out}/R_{\rm side}$.

Fig. 18: The same as in Fig. 13, but for the ratio $R_{\rm out}/R_{\rm side}$.

Fig. 1

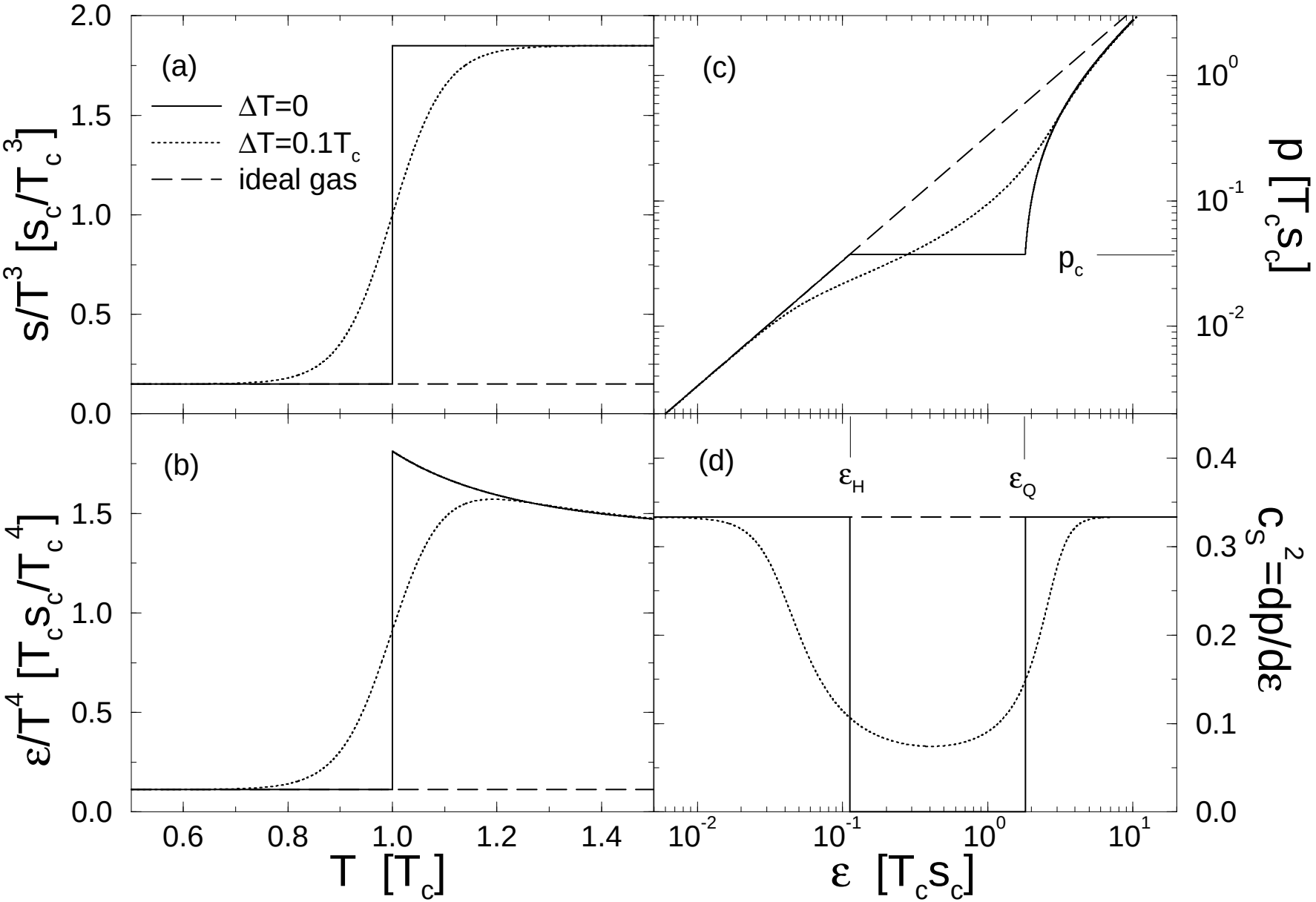
(a)
ΔT=0
ΔT=0.1T_c
ideal gas
s/T^3 [s_c/T_c^3]
(b)
ε/T^4 [T_c s_c/T_c^4]
T [T_c]
(c)
p_c
p [T_c s_c]
(d)
ε_H
ε_Q
c_s^2=dp/dε
ε [T_c s_c]

Fig. 2

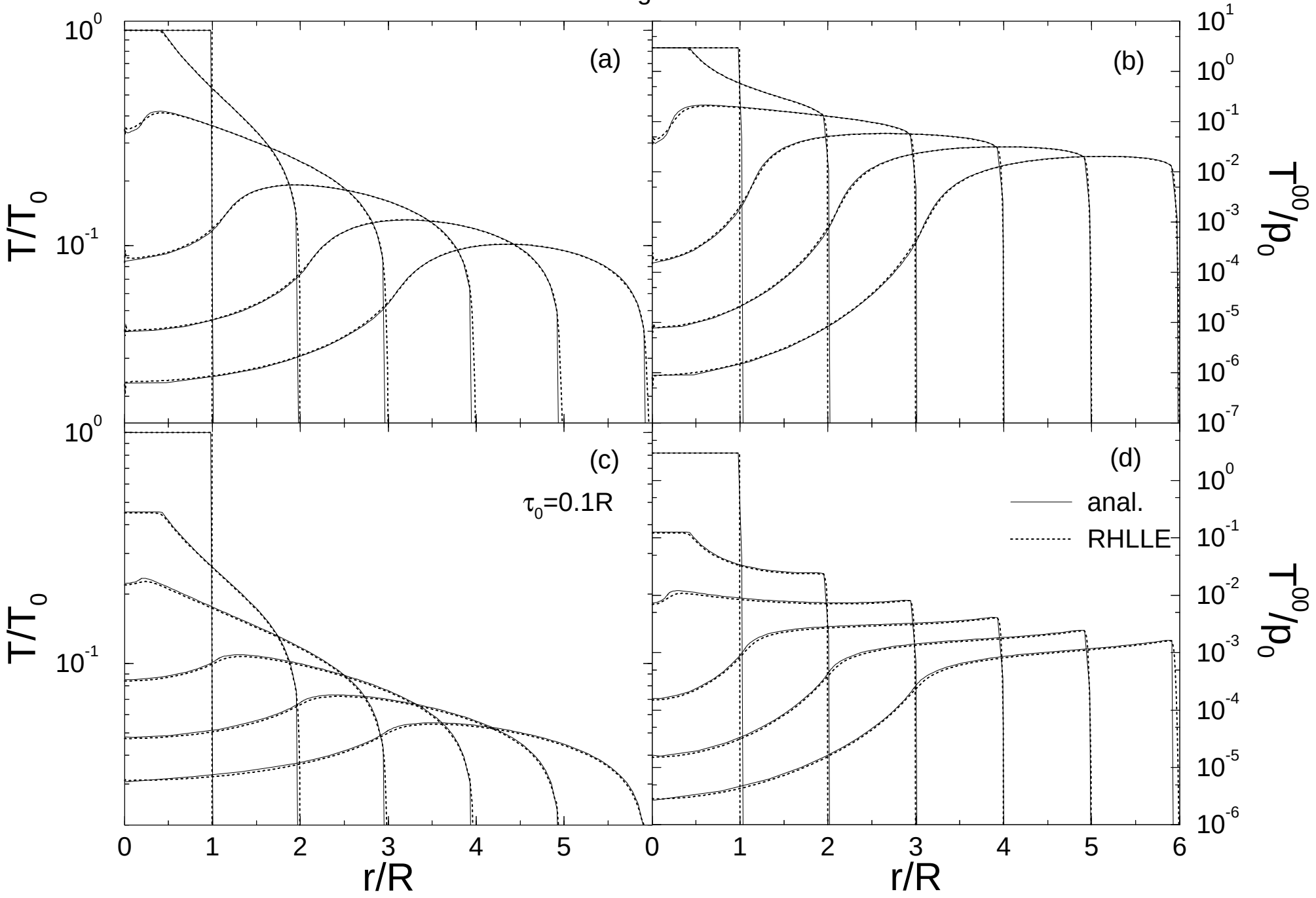

Fig. 3

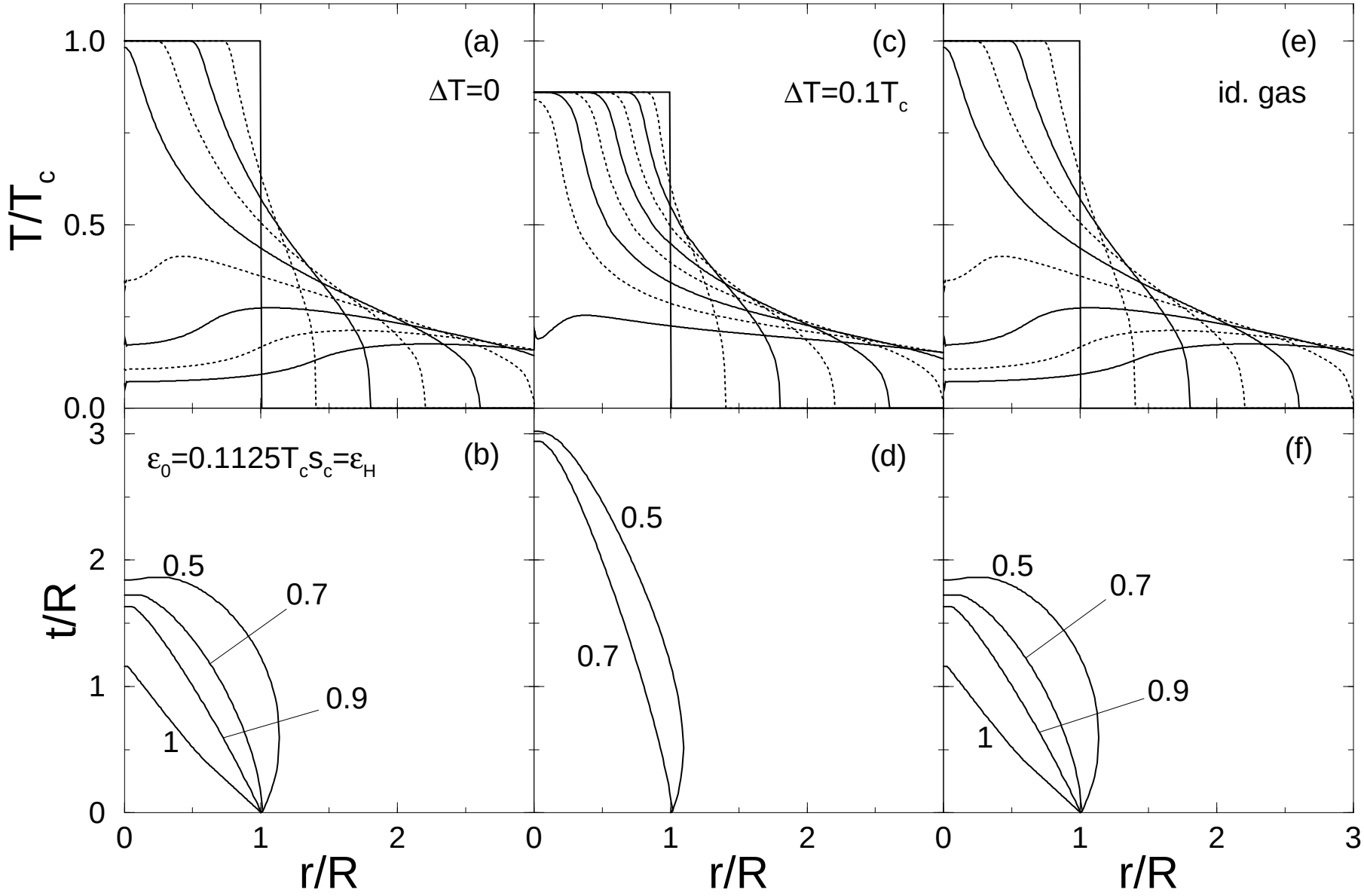
(a)
ΔT=0
(c)
ΔT=0.1T_c
(e)
id. gas
T/T_c
1.0
0.5
0.0
(b)
ε_0=0.1125T_cs_c=ε_H
(d)
(f)
t/R
3
2
1
0
0.5
0.7
0.9
1
0.5
0.7
0.5
0.7
0.9
1
0
1
2
0
1
2
0
1
2
3
r/R
r/R
r/R

Fig. 4

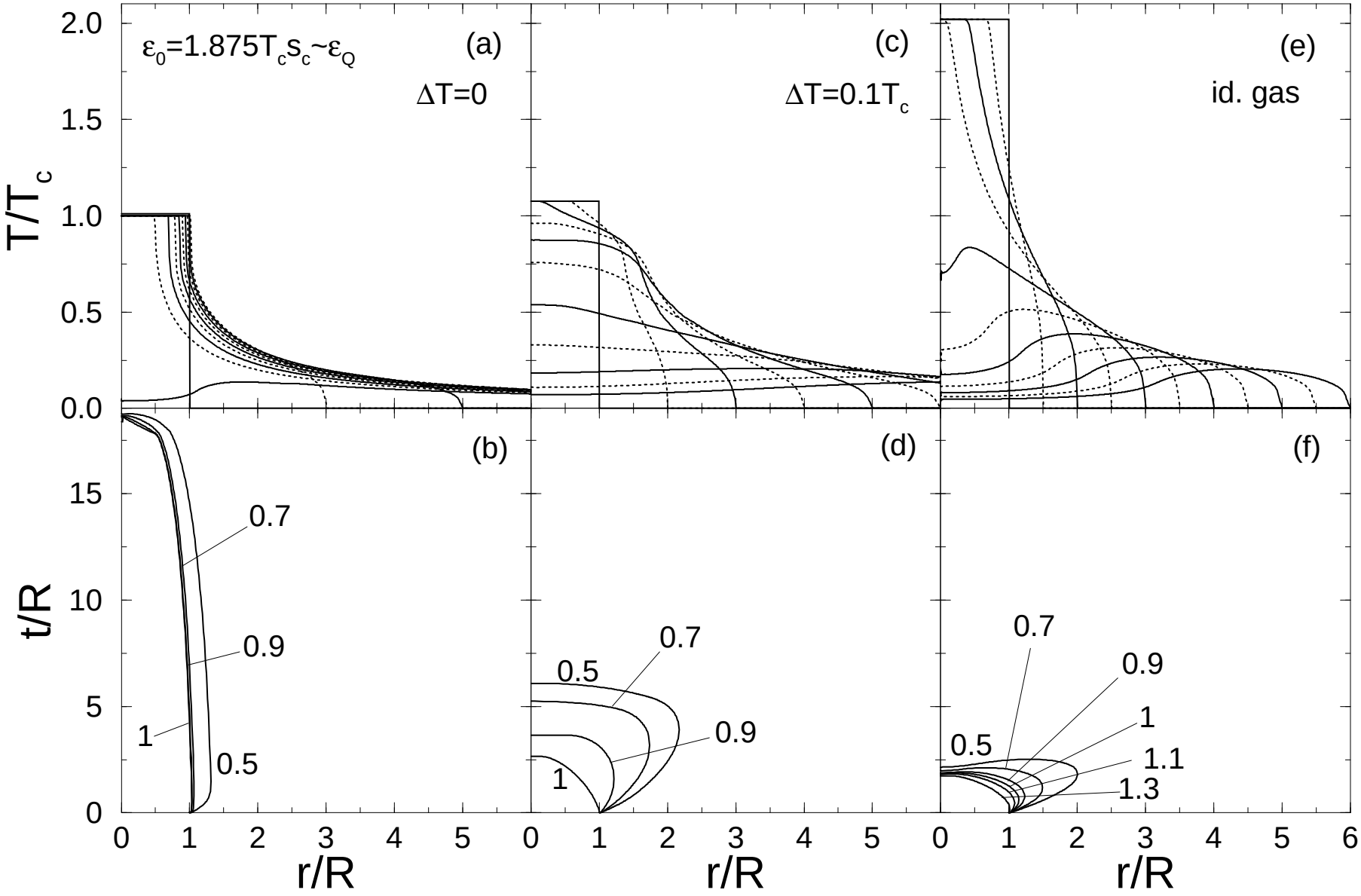
ε0=1.875TcsccεQ
(a)
ΔT=0
(c)
ΔT=0.1Tc
(e)
id. gas
T/Tc
(b)
(d)
(f)
t/R
r/R
r/R
r/R
0.7
0.9
1
0.5
0.5
0.7
0.9
1
0.7
0.9
1
1.1
1.3
0.5

Fig. 5

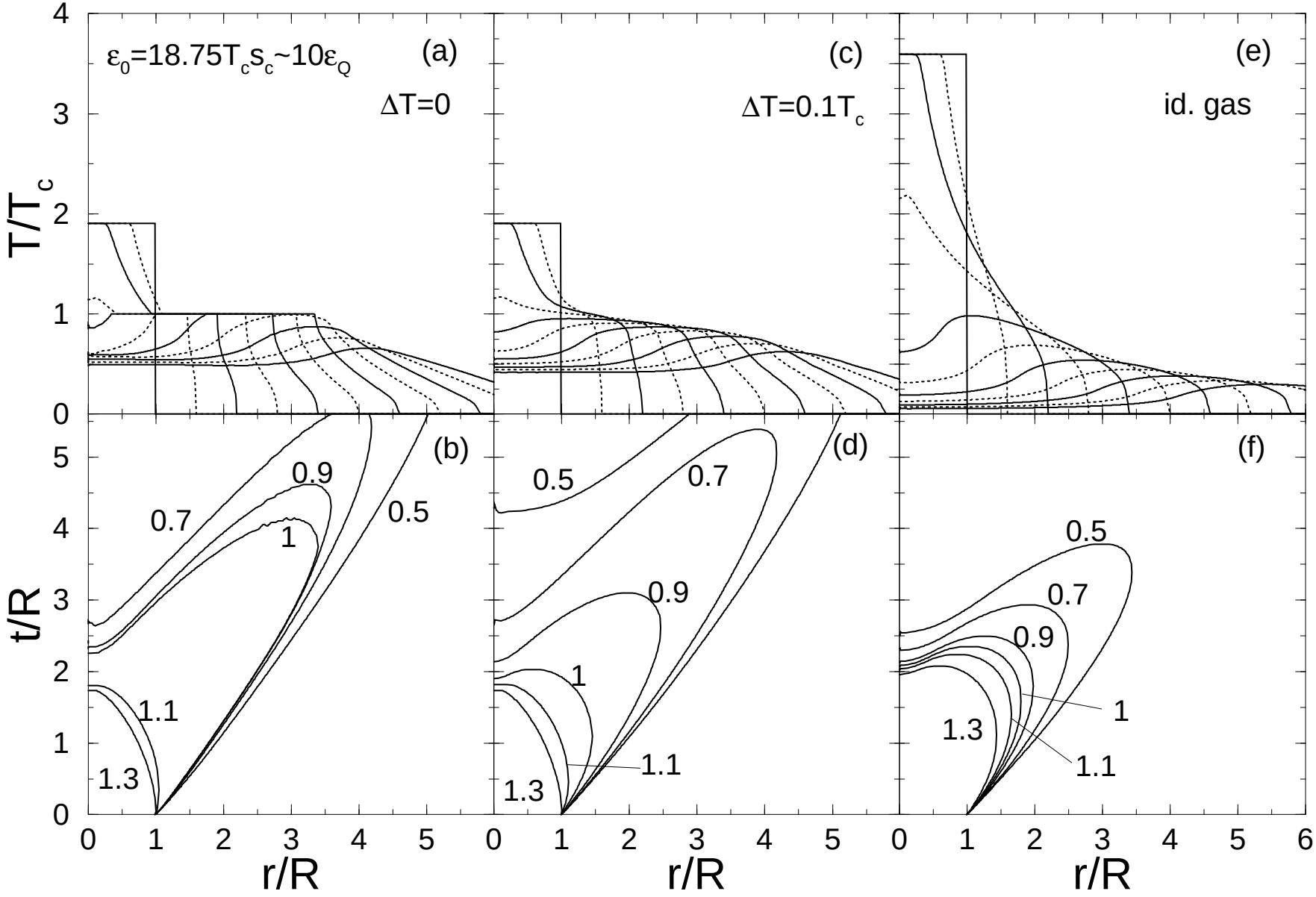
ε0=18.75TcSc~10εQ
(a)
ΔT=0
(c)
ΔT=0.1Tc
(e)
id. gas
T/Tc
(b)
(d)
(f)
t/R
r/R
0.5
0.7
0.9
1
1.1
1.3

Fig. 6

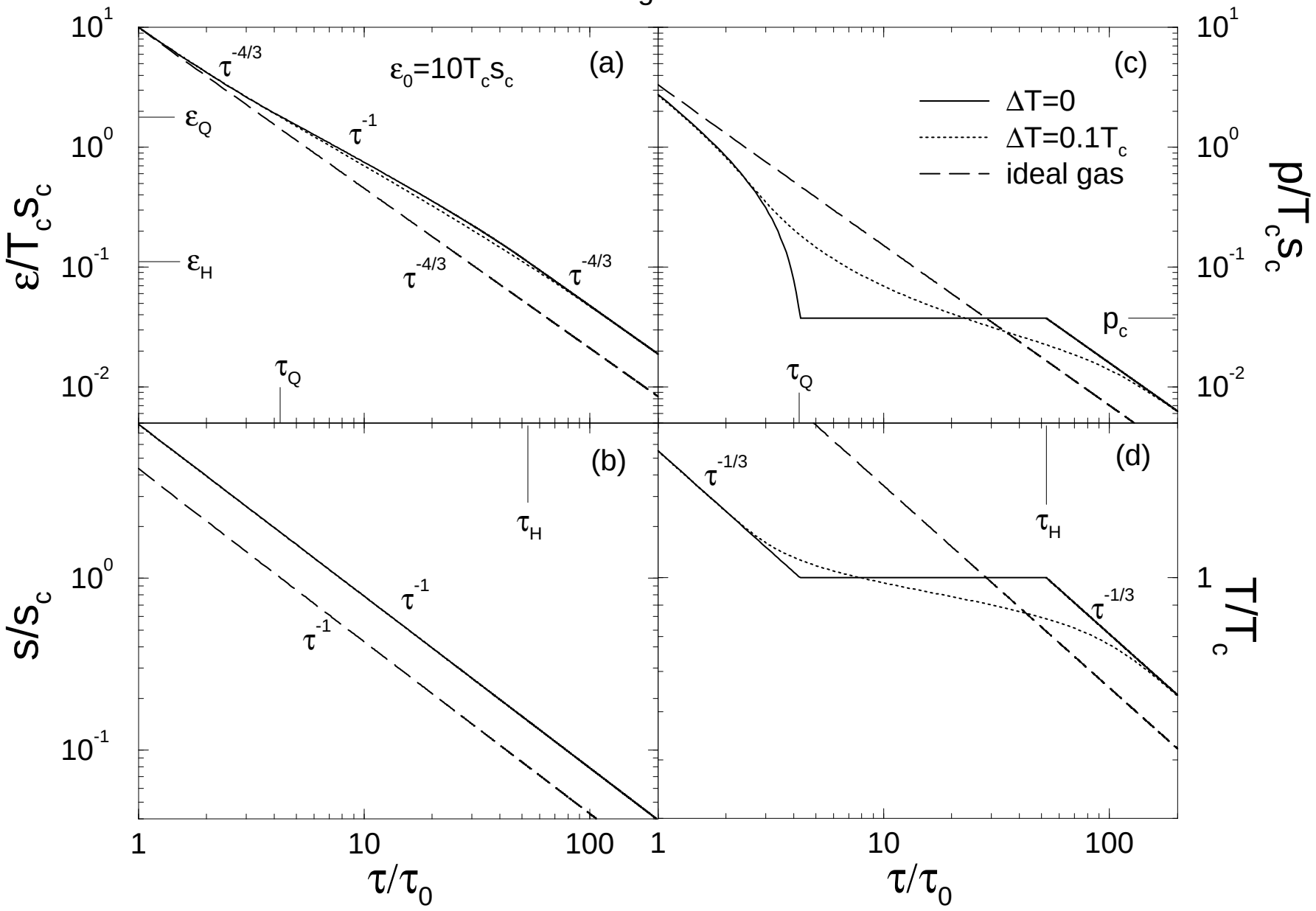
(a)
(b)
(c)
(d)
$\varepsilon_0=10T_cs_c$
ε_Q
ε_H
τ_Q
τ_H
$\tau^{-4/3}$
τ^{-1}
$\tau^{-1/3}$
p_c
$\Delta T=0$
$\Delta T=0.1T_c$
ideal gas
ε/T_cs_c
s/s_c
p/T_cs_c
T/T_c
τ/τ_0
10^1
10^0
10^{-1}
10^{-2}
1
10
100

Fig. 7

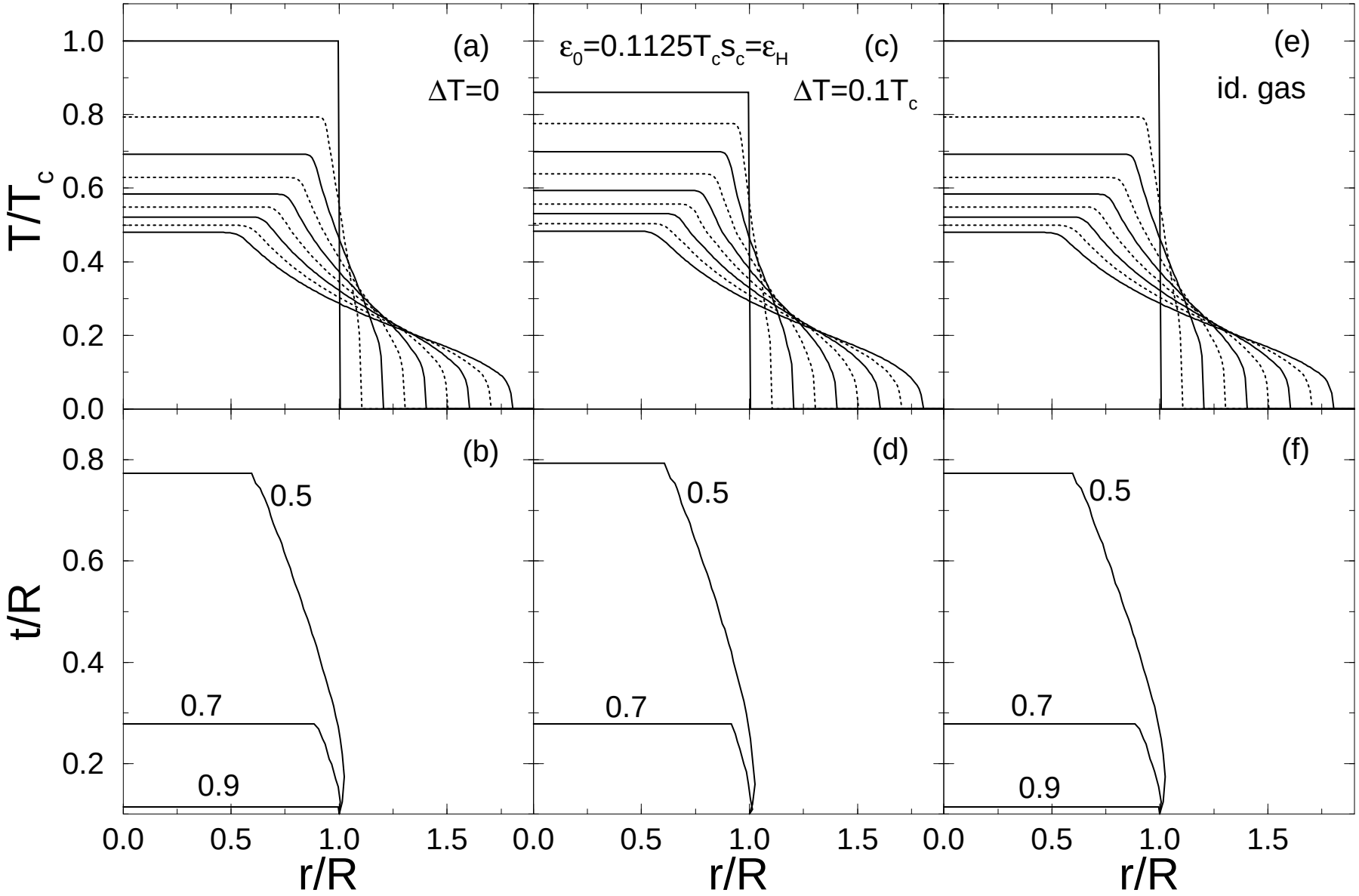
(a)
ΔT=0
ε0=0.1125TcsC=εH
(c)
ΔT=0.1Tc
(e)
id. gas
T/Tc
(b)
(d)
(f)
t/R
0.5
0.7
0.9
r/R
0.0
0.2
0.4
0.6
0.8
1.0
1.5

Fig. 8

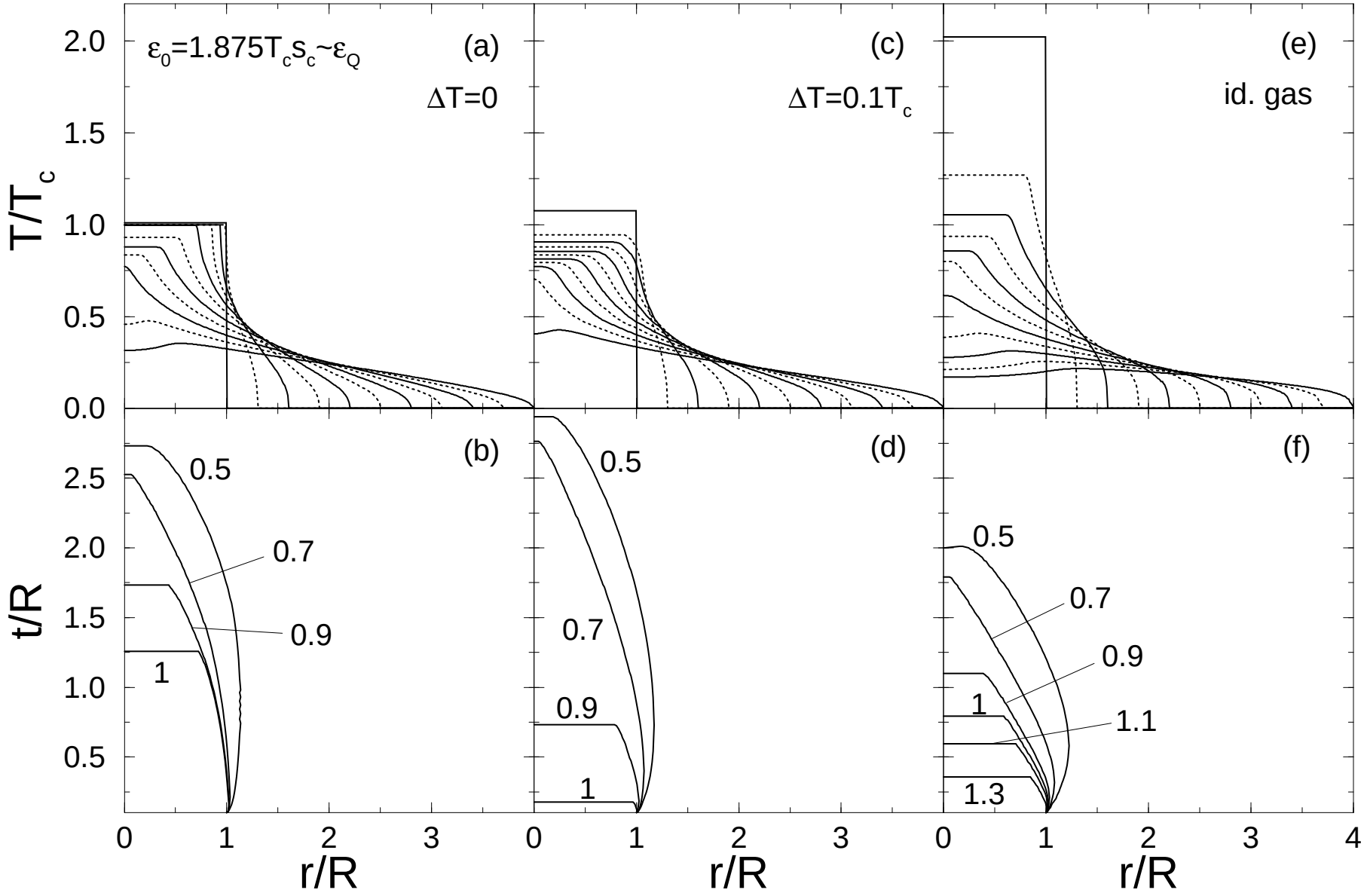
ε0=1.875Tcsc~εQ
(a)
ΔT=0
(c)
ΔT=0.1Tc
(e)
id. gas
(b)
(d)
(f)
T/Tc
t/R
r/R
r/R
r/R
0.5
0.7
0.9
1
0.5
0.7
0.9
1
0.5
0.7
0.9
1
1.1
1.3

Fig. 9

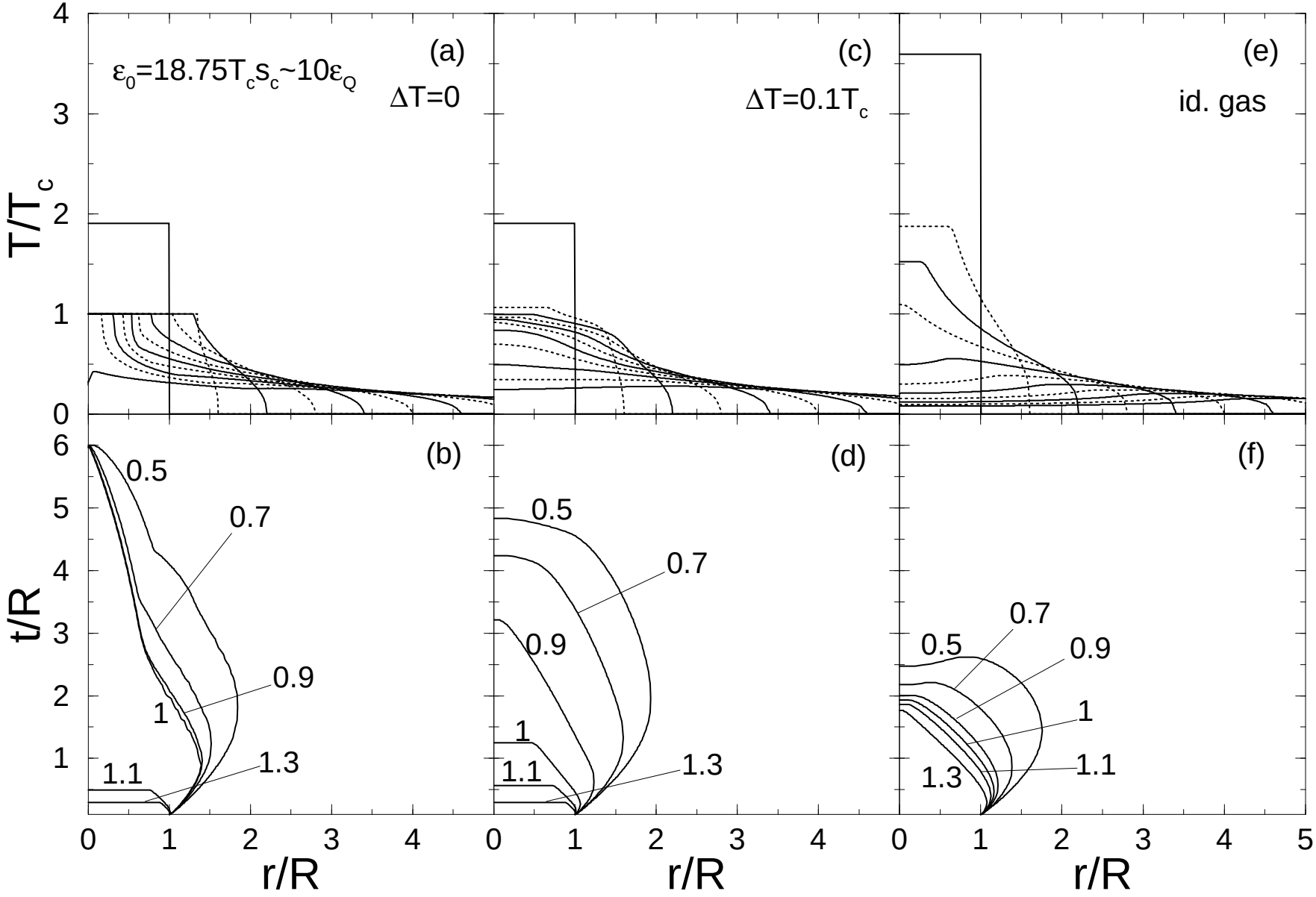
(a)
$\varepsilon_0=18.75T_cs_c\sim10\varepsilon_Q$
$\Delta T=0$
(c)
$\Delta T=0.1T_c$
(e)
id. gas
T/T$_c$
(b)
(d)
(f)
0.5
0.7
0.9
1
1.1
1.3
t/R
r/R
r/R
r/R

Fig. 10

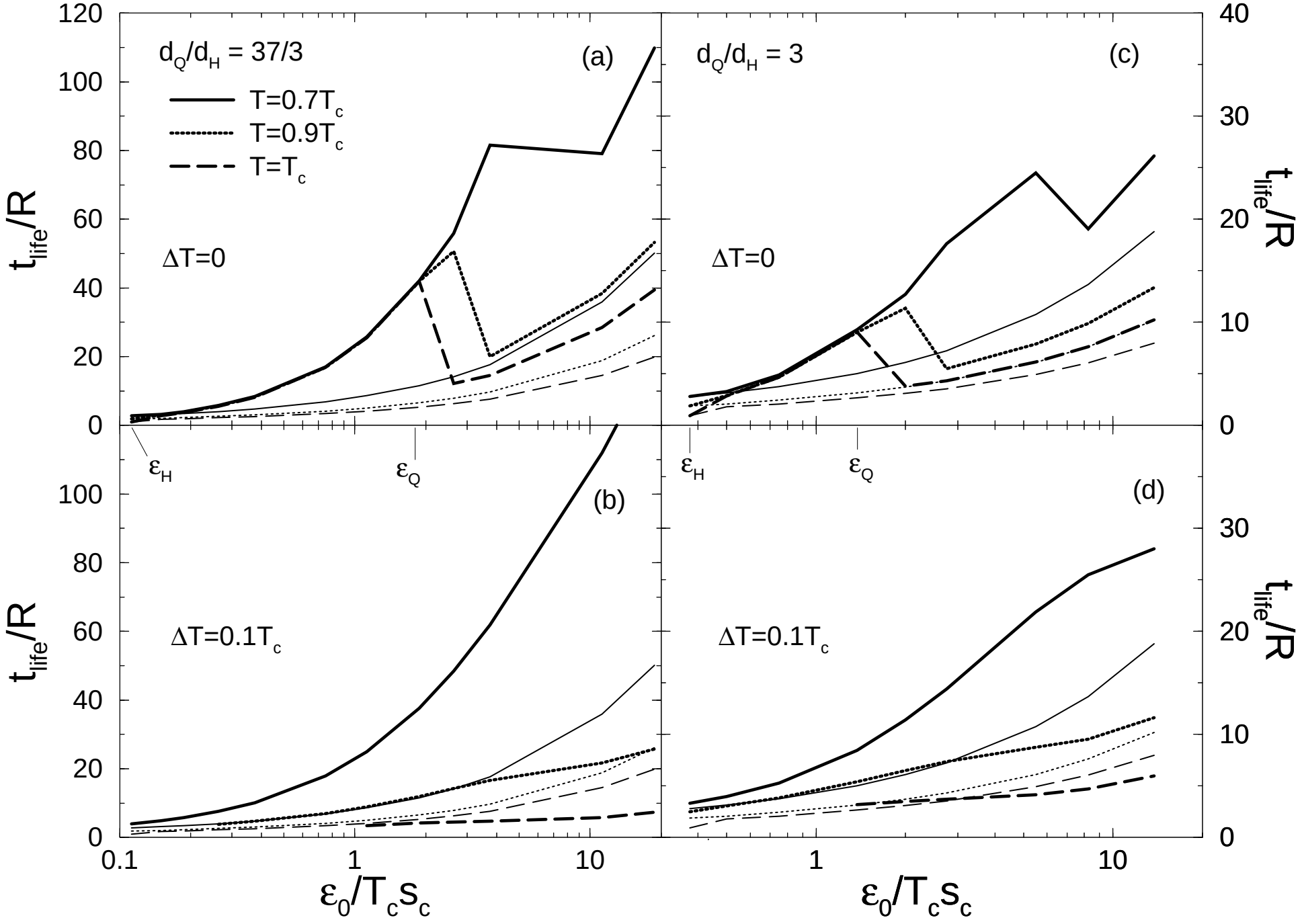
d_Q/d_H = 37/3
(a)
T=0.7T_c
T=0.9T_c
T=T_c
ΔT=0
d_Q/d_H = 3
(c)
ΔT=0
ε_H
ε_Q
(b)
ΔT=0.1T_c
(d)
ΔT=0.1T_c
t_life/R
ε_0/T_cs_c
0
20
40
60
80
100
120
10
30
0.1
1
10

Fig. 11

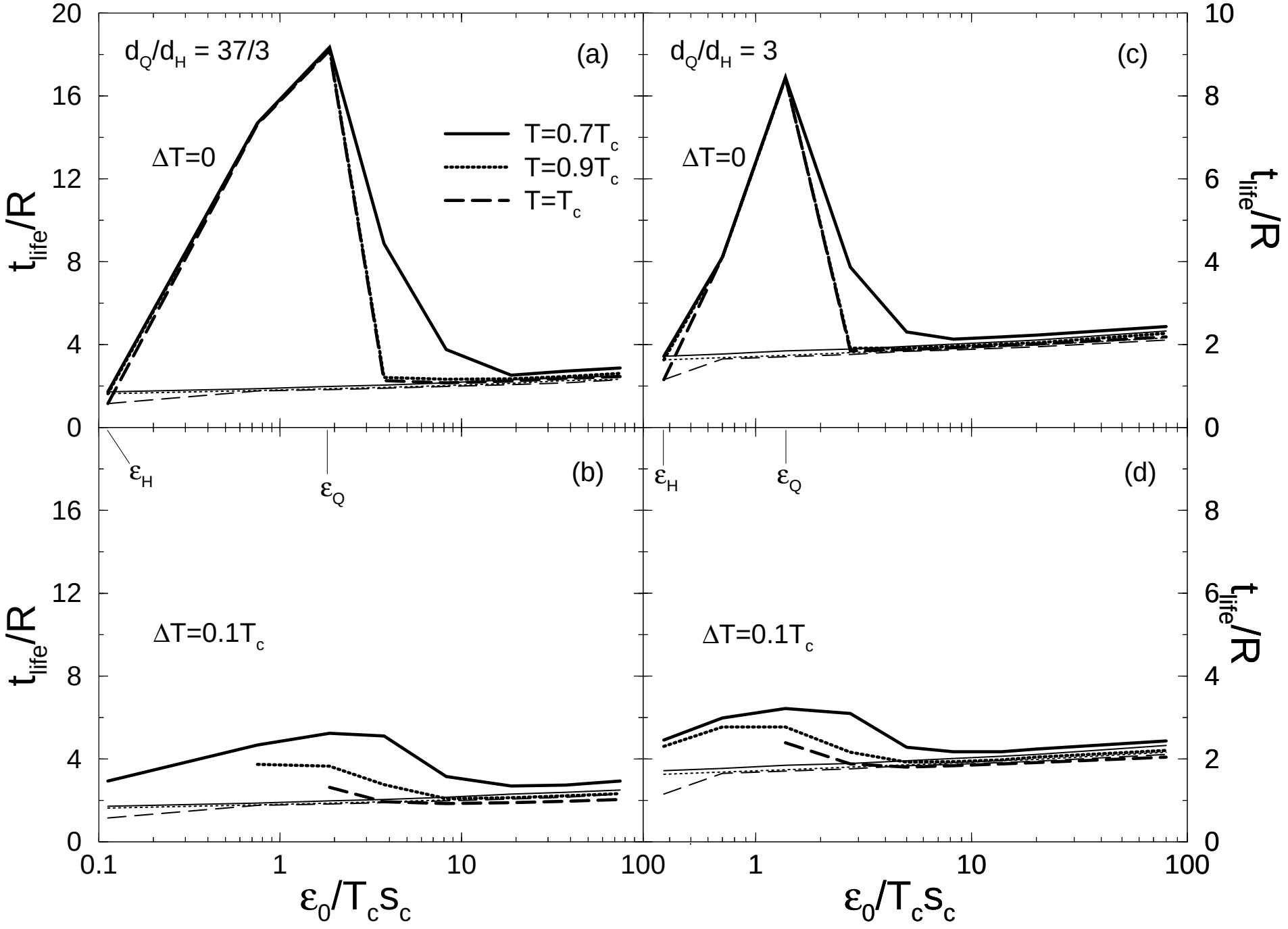
d_Q/d_H = 37/3
(a)
d_Q/d_H = 3
(c)
$\Delta T=0$
$T=0.7T_c$
$T=0.9T_c$
$T=T_c$
t_{life}/R
ε_H
ε_Q
(b)
(d)
$\Delta T=0.1T_c$
ε_0/T_cs_c
0.1
1
10
100
0
2
4
6
8
10
12
16
20

Fig. 12

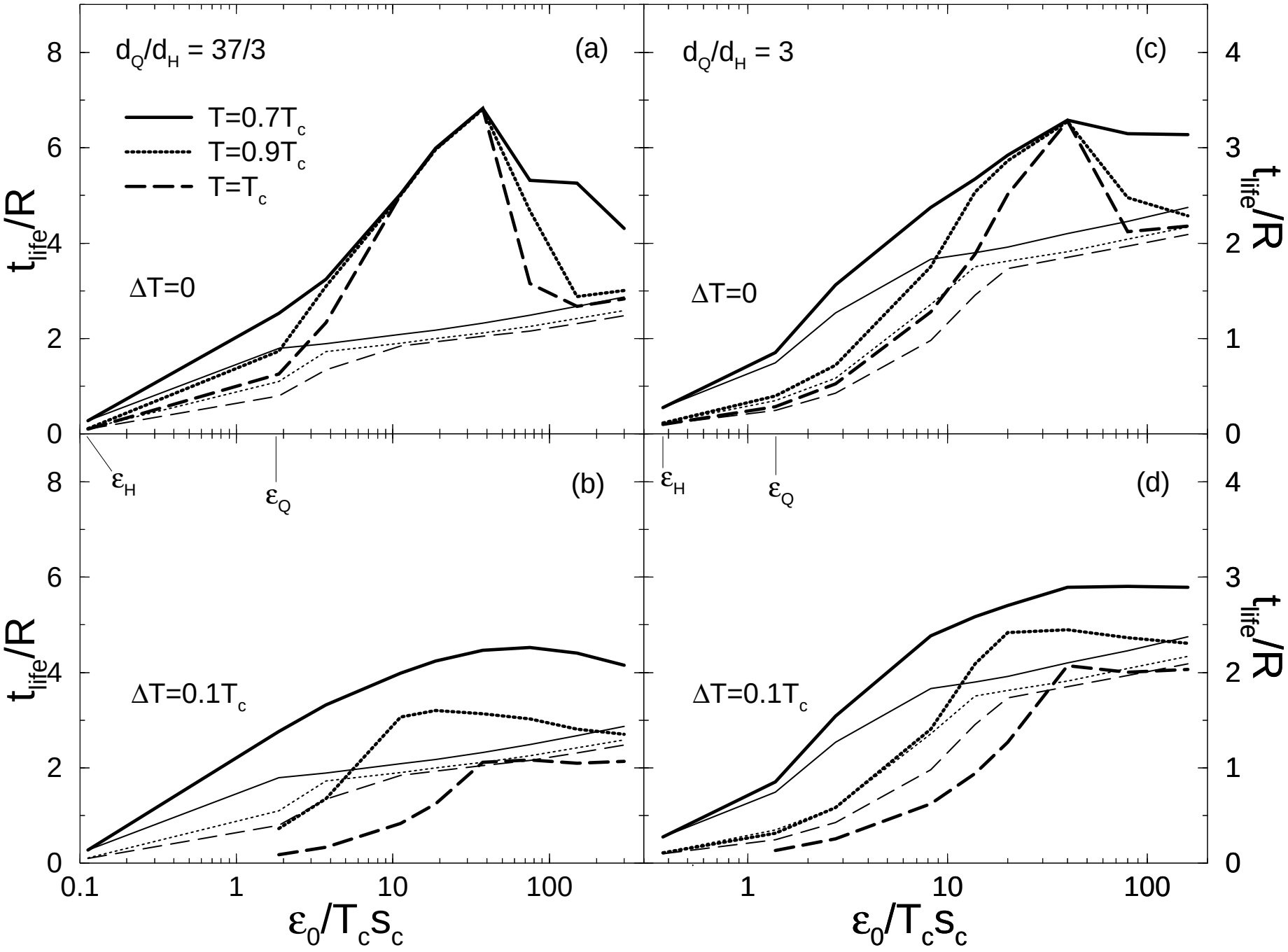
d_Q/d_H = 37/3
(a)
d_Q/d_H = 3
(c)
T=0.7T_c
T=0.9T_c
T=T_c
ΔT=0
ΔT=0
t_{life}/R
ε_H
ε_Q
(b)
(d)
ΔT=0.1T_c
ΔT=0.1T_c
ε_0/T_cs_c
0.1
1
10
100

Fig. 13

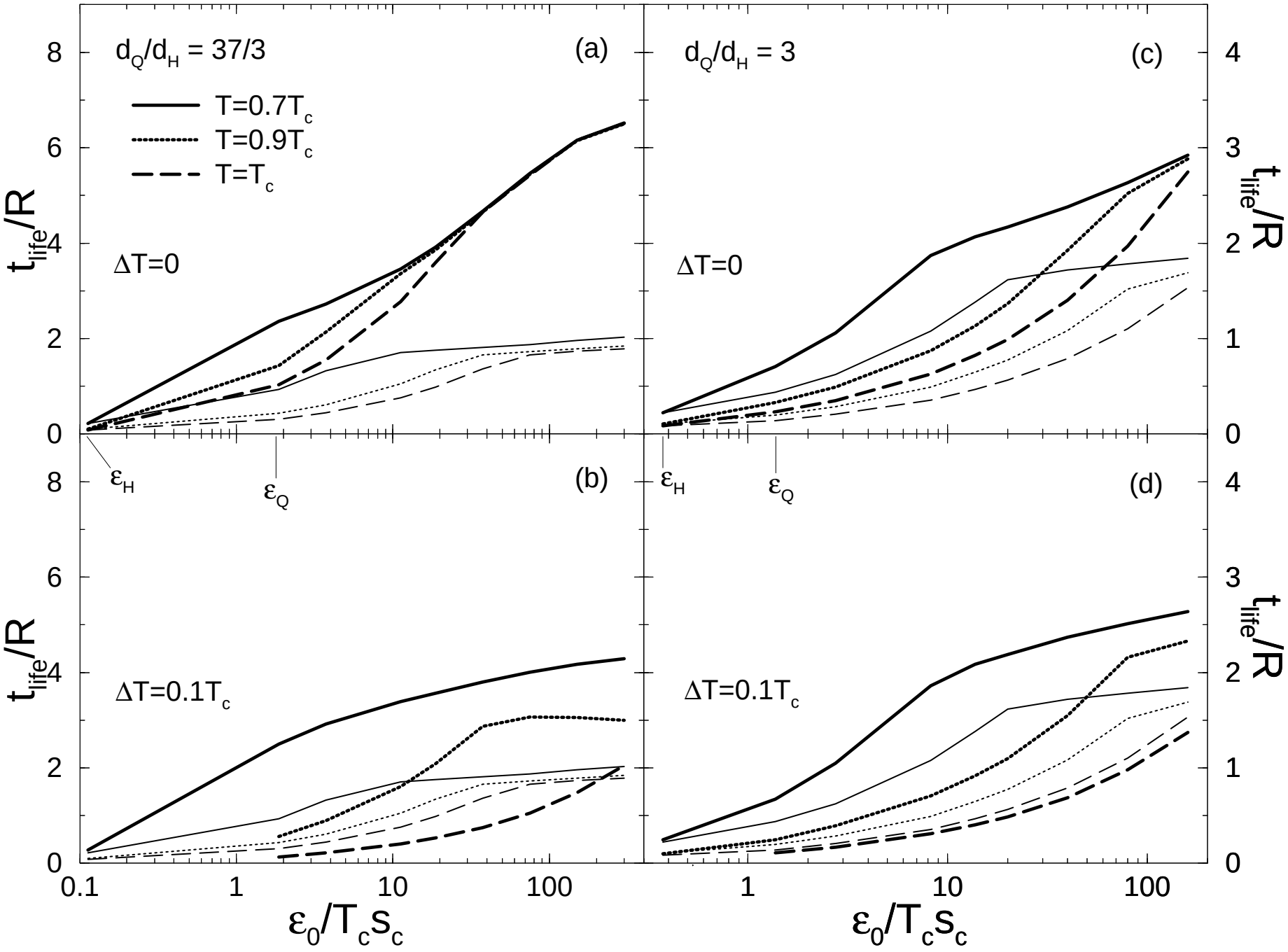
d_Q/d_H = 37/3
(a)
T=0.7T_c
T=0.9T_c
T=T_c
ΔT=0
d_Q/d_H = 3
(c)
ΔT=0
ε_H
ε_Q
(b)
(d)
ΔT=0.1T_c
ΔT=0.1T_c
t_life/R
ε_0/T_cs_c
0.1
1
10
100
0
2
4
6
8
1
2
3
4

Fig. 14

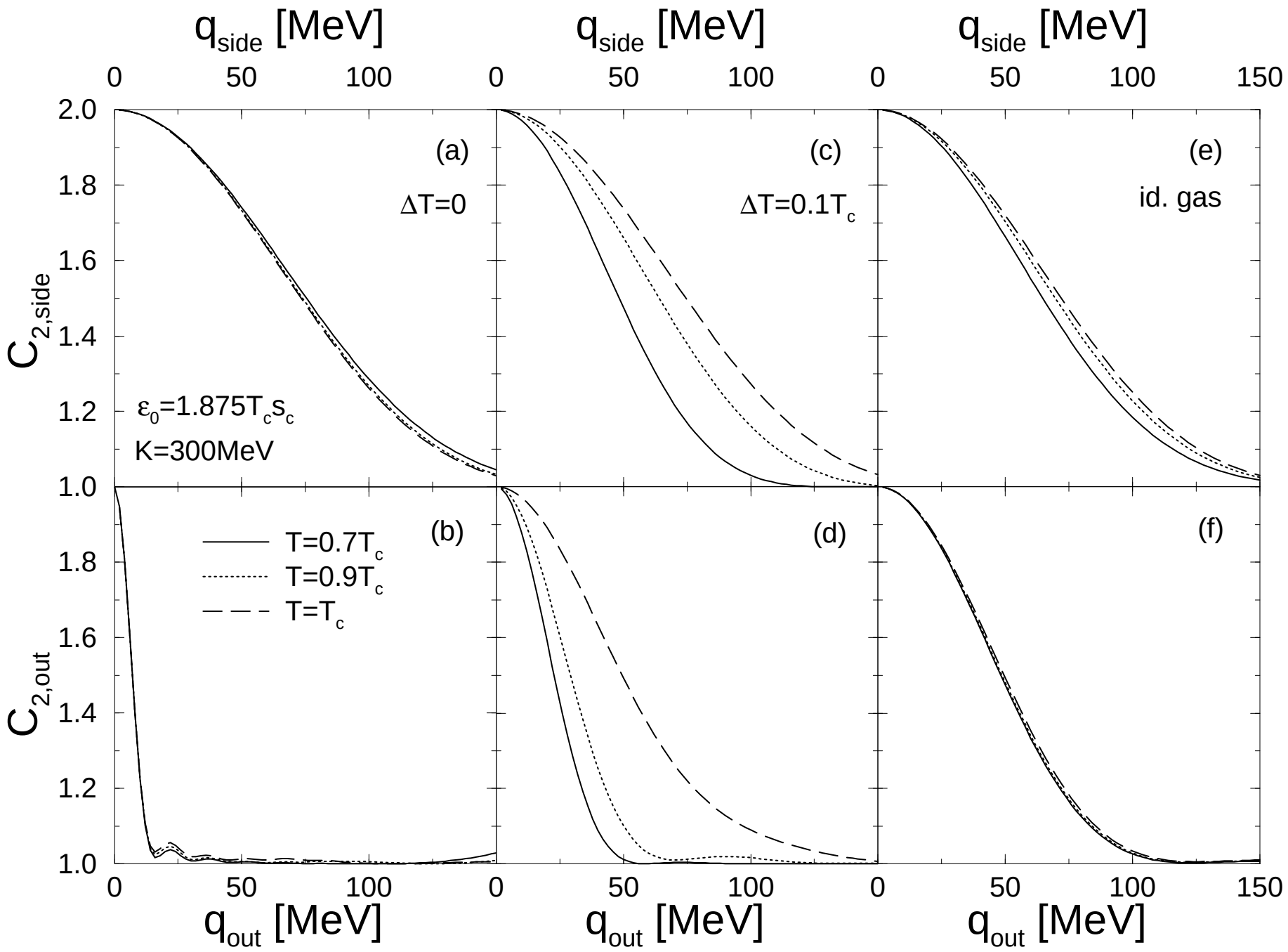
q_{side} [MeV]
q_{out} [MeV]
$C_{2,side}$
$C_{2,out}$
(a)
$\Delta T=0$
$\varepsilon_0=1.875T_cs_c$
K=300MeV
(b)
T=0.7T_c
T=0.9T_c
T=T_c
(c)
$\Delta T=0.1T_c$
(d)
(e)
id. gas
(f)

Fig. 15

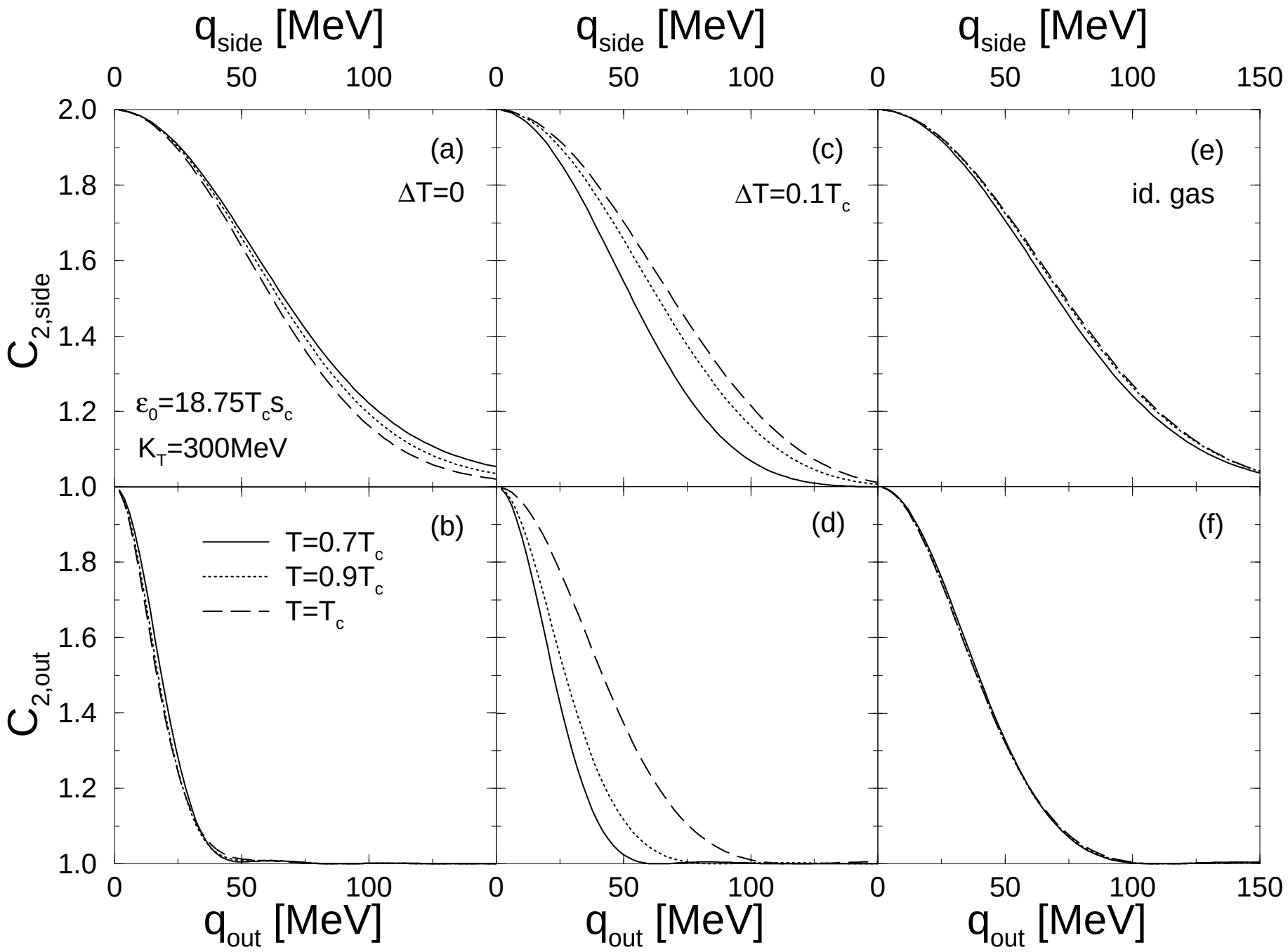
q_{side} [MeV]
q_{out} [MeV]
$C_{2,side}$
$C_{2,out}$
(a)
$\Delta T=0$
(c)
$\Delta T=0.1T_c$
(e)
id. gas
$\varepsilon_0=18.75T_cs_c$
$K_T=300$MeV
(b)
(d)
(f)
$T=0.7T_c$
$T=0.9T_c$
$T=T_c$

Fig. 16

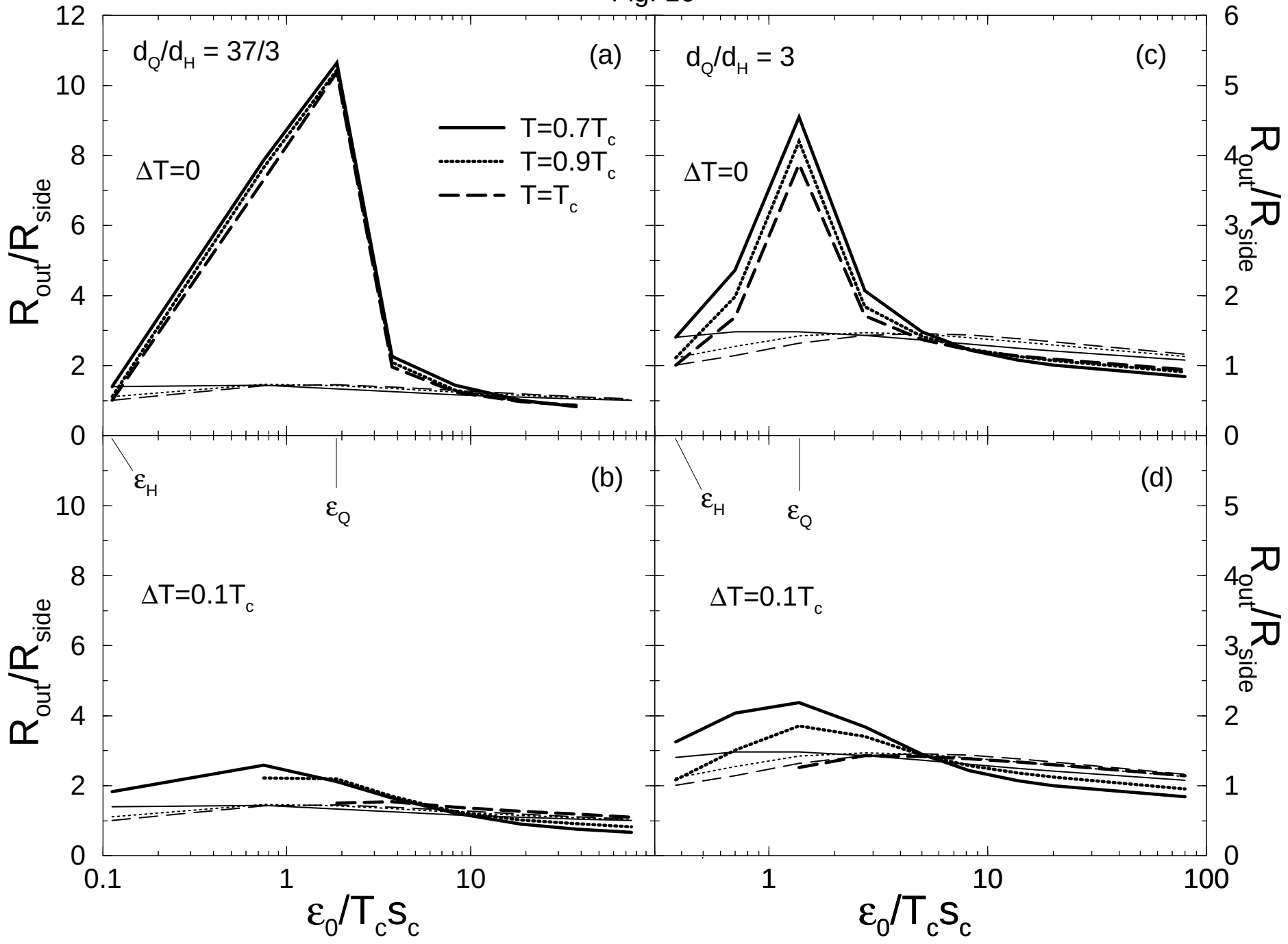
d_Q/d_H = 37/3
(a)
d_Q/d_H = 3
(c)
ΔT=0
ΔT=0
$T=0.7T_c$
$T=0.9T_c$
$T=T_c$
ε_H
ε_Q
(b)
(d)
$\Delta T=0.1T_c$
$\Delta T=0.1T_c$
R_{out}/R_{side}
ε_0/T_cs_c
0.1
1
10
100

Fig. 17

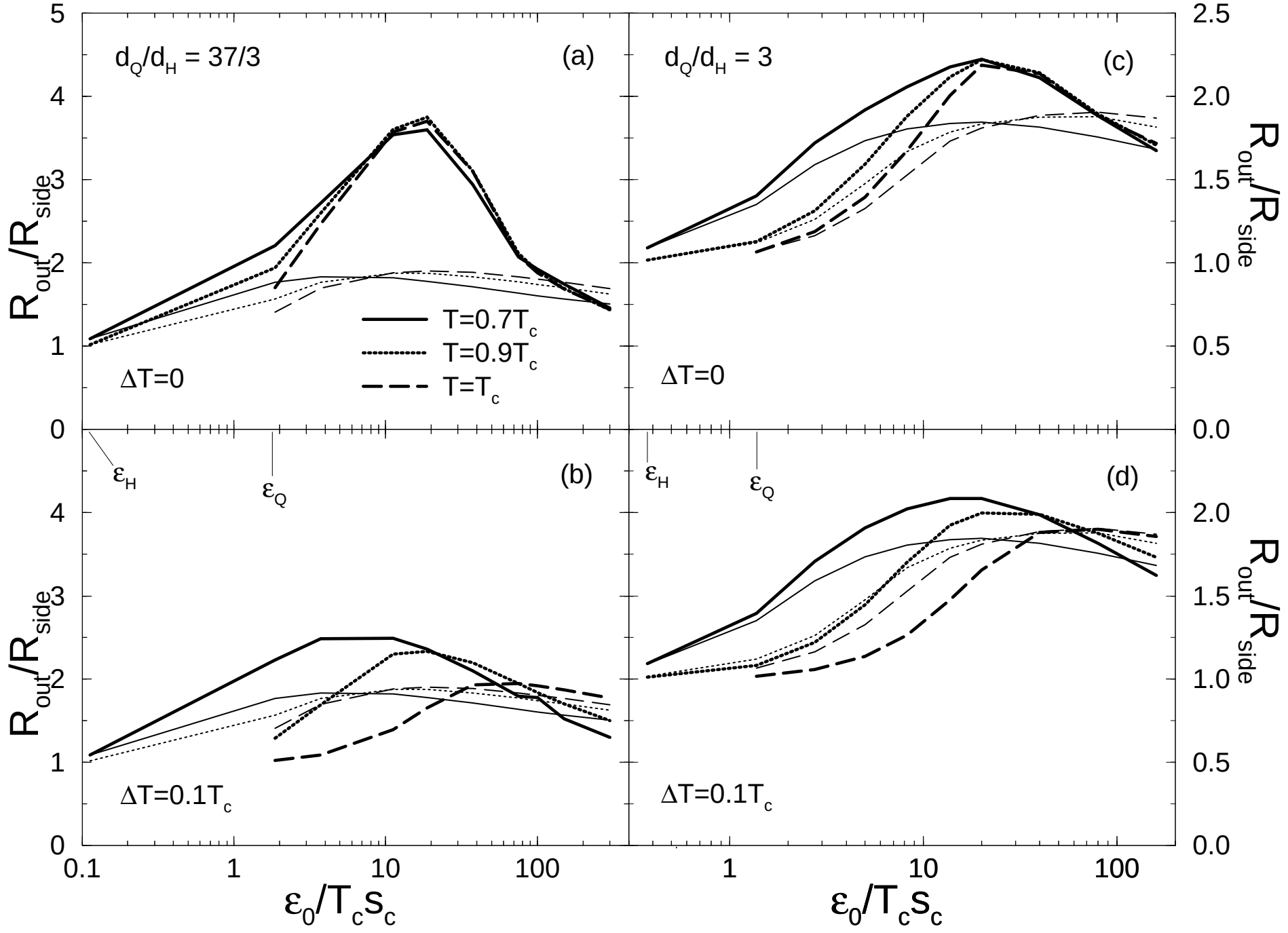
d_Q/d_H = 37/3
(a)
d_Q/d_H = 3
(c)
$T=0.7T_c$
$T=0.9T_c$
$T=T_c$
$\Delta T=0$
$\Delta T=0$
ε_H
ε_Q
(b)
(d)
$\Delta T=0.1T_c$
$\Delta T=0.1T_c$
R_{out}/R_{side}
ε_0/T_cs_c

Fig. 18

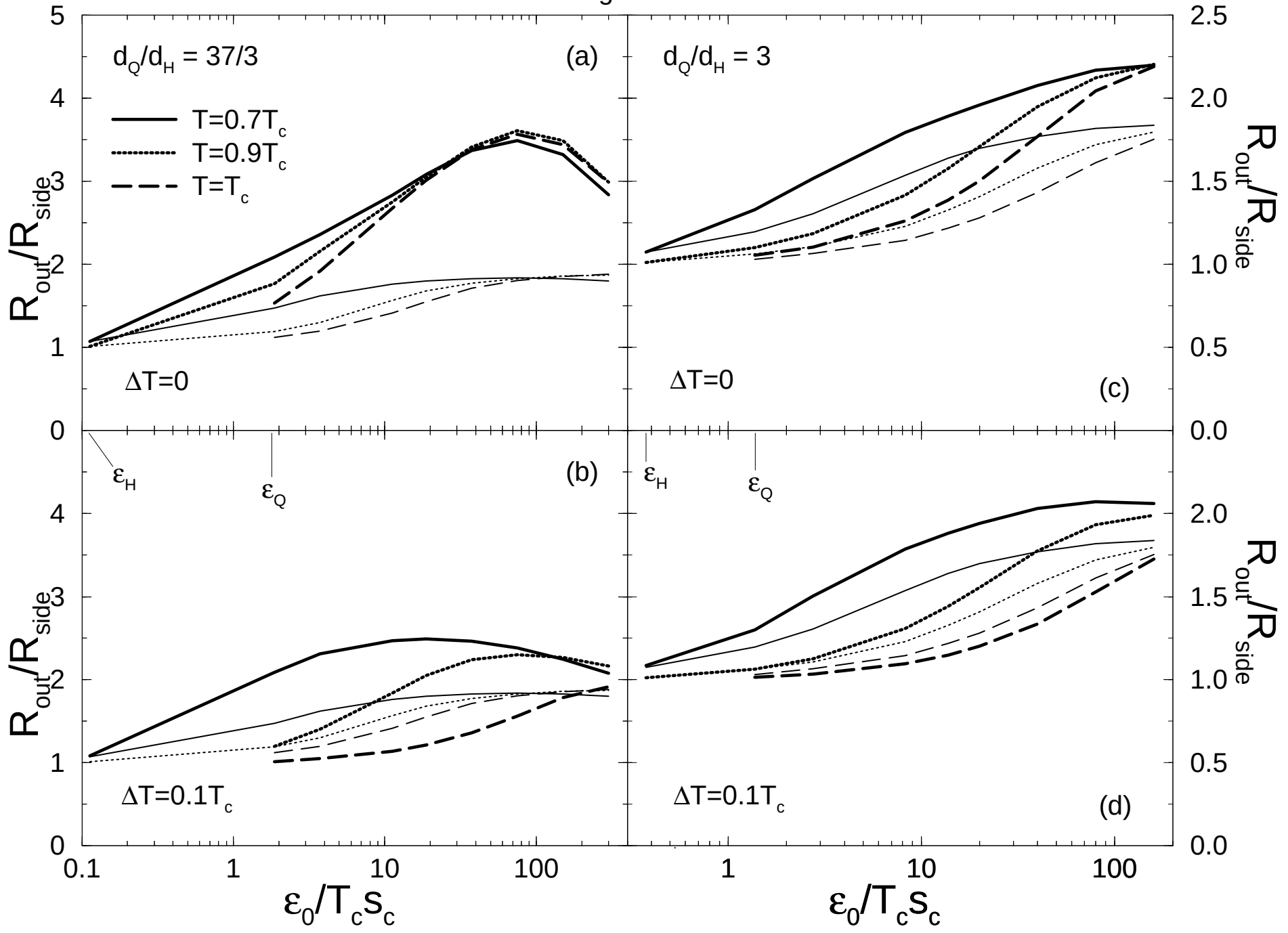
d_Q/d_H = 37/3
(a)
T=0.7T_c
T=0.9T_c
T=T_c
ΔT=0
d_Q/d_H = 3
(c)
ΔT=0
ε_H
ε_Q
(b)
ΔT=0.1T_c
(d)
ΔT=0.1T_c
R_{out}/R_{side}
ε_0/T_cs_c
0.1
1
10
100
0
1
2
3
4
5
0.0
0.5
1.0
1.5
2.0
2.5